REPORT DOCUMENTATION PAGE

1. REPORT DATE *(DD-MM-YYYY)* 2/25/2011	2. REPORT TYPE Final Technical Report		3. DATES COVERED *(From - To)* 2/15/2008-11/30/2010
4. TITLE AND SUBTITLE Cyanate Ester Resin Modified with Nano-particles for Inclusion in Continuous Fiber Reinforced Composites			5a. CONTRACT NUMBER
			5b. GRANT NUMBER FA9550-08-1-0033
			5c. PROGRAM ELEMENT NUMBER
6. AUTHOR(S) Dr. Michael R. Kessler and Dr. Prashanth Badrinarayanan 2220 Hoover Hall Iowa State University Ames, IA 50011-2300			5d. PROJECT NUMBER
			5e. TASK NUMBER
			5f. WORK UNIT NUMBER
7. PERFORMING ORGANIZATION NAME(S) AND ADDRESS(ES) Iowa State University 1350 Beardshear Hall Ames IA 50011-2025			8. PERFORMING ORGANIZATION REPORT NUMBER 421-20-03
9. SPONSORING / MONITORING AGENCY NAME(S) AND ADDRESS(ES) USAF, AFRL DUNS 143574726 AF OFFICE OF SCIENTIFIC RESEARCH 875 N. RANDOLPH ST. ROOM 3112 ARLINGTON VA 22203			10. SPONSOR/MONITOR'S ACRONYM(S) AFOSR
			11. SPONSOR/MONITOR'S REPORT NUMBER(S) AFRL-OSR-VA-TR-2012-0448

12. DISTRIBUTION / AVAILABILITY STATEMENT

A

13. SUPPLEMENTARY NOTES

14. ABSTRACT
The mismatch in coefficient of thermal expansion (CTE) between the polymer matrix and low CTE carbon fibers causes development of residual stresses in polymer matrix composites (PMCs) that can lead to micro cracking and failure. This report describes the development of hybrid polymer composites comprising of a unique low viscosity bisphenol E cyanate ester resin (BECy) resin reinforced with macro scale carbon fibers and negative CTE nanoparticles. Polymer nanocomposites were developed with negative CTE fillers such as multiwalled carbon nanotubes (CNTs) and zirconium tungstate (ZrW_2O_8). The BECy/ ZrW_2O_8 nanocomposites were identified as the most promising candidates for development of hybrid composites and a silane surface treatment strategy was developed to improve the compatibility of the ZrW_2O_8 nanoparticles with the polymer matrix. The hybrid composites were prepared with 30 wt. % unidirectional carbon fibers and various loadings of ZrW_2O_8 nanoparticles. Incorporation of 20 vol. % ZrW_2O_8 nanoparticles was found to result in a 75 % reduction in the normal and in plane CTE of 10 ply symmetric composites. Furthermore, the warpage in 2 ply unsymmetrical composites was found to decrease systematically with nanoparticle loading due to a reduction in the CTE mismatch between the matrix and fiber reinforcements.

15. SUBJECT TERMS

16. SECURITY CLASSIFICATION OF:			17. LIMITATION OF ABSTRACT	18. NUMBER OF PAGES	19a. NAME OF RESPONSIBLE PERSON Michael R. Kessler
a. REPORT	b. ABSTRACT	c. THIS PAGE		54	19b. TELEPHONE NUMBER *(include area code)* 515-294-3101

Cyanate Ester Resins Modified with Nano-particles for Inclusion in Continuous Fiber Reinforced Composites

Michael R. Kessler and Prashanth Badrinarayanan
Materials Science and Engineering, Iowa State University
2220 Hoover Hall
Ames, IA 50011-2300
Phone: 515-294-3101
Fax: 515-294-5444
mkessler@iastate.edu

Index **Pg.no**

Abstract/ Executive Summary

The mismatch in coefficient of thermal expansion (CTE) between the polymer matrix and low CTE carbon fibers causes development of residual stresses in polymer matrix composites (PMCs) that can lead to micro cracking and failure. This report describes the development of hybrid polymer composites comprising of a unique low viscosity bisphenol E cyanate ester resin (BECy) resin reinforced with macro scale carbon fibers and negative CTE nanoparticles.

Polymer nanocomposites were developed with negative CTE fillers such as multiwalled carbon nanotubes (CNTs) and zirconium tungstate (ZrW_2O_8). The BECy/ ZrW_2O_8 nanocomposites were identified as the most promising candidates for development of hybrid composites and a silane surface treatment strategy was developed to improve the compatibility of the ZrW_2O_8 nanoparticles with the polymer matrix. The hybrid composites were prepared with 30 wt. % unidirectional carbon fibers and various loadings of ZrW_2O_8 nanoparticles. Incorporation of 20 vol. % ZrW_2O_8 nanoparticles was found to result in a 75 % reduction in the normal and in plane CTE of 10 ply symmetric composites. Furthermore, the warpage in 2 ply unsymmetrical composites was found to decrease systematically with nanoparticle loading due to a reduction in the CTE mismatch between the matrix and fiber reinforcements.

Cumulative Lists of People Involved in the Research Effort

1. Michael R. Kessler
2. Prashanth Badrinarayanan
3. Karen Haman
4. Ben Mac Murray
5. Josh Leonard

Publications Stemming From the Research Effort

Journal Articles

- K.J. Haman, P. Badrinarayanan, M.R. Kessler "Effect of zirconium tungstate filler particles on the cure behavior of a cyanate ester resin ", *ACS Applied Materials and Interfaces*, 1, 1190-1195 (2009).
- P. Badrinarayanan, B.C. Mac Murray, M.R. Kessler "Zirconium tungstate reinforced cyanate ester composites with enhanced dimensional stability", *Journal of Materials Research*, 24, 2235-2242 (2009).
- P. Badrinarayanan, J. Leonard, M.R. Kessler "Enhanced reaction kinetics and impact strength of cyanate ester reinforced with multiwalled carbon nanotubes", *Journal of Nanoscience and Nanotechnology*, In Press, (2010).
- P. Badrinarayanan and M.R. Kessler, "Zirconium Tungstate Cyanate Ester Nanocomposites with Tailored Thermal Expansivity", *Composites Science and Technology*, Under Review, 2011.

Invited Workshop Presentations

- M. R. Kessler and P. Badrinarayanan, "Cyanate Ester Based Hybrid Composites with Tailored Thermal Expansion" AFOSR 2011 Low Density Materials Program Review, January 4-5, 2011. Arlington, VA.
- M. R. Kessler, "Cyanate Ester Resins Modified with Nano-Particles for Inclusion in Continuous Fiber Reinforced Composites" AFOSR 2009 Low Density Materials Program Review, October 8-9, 2009. Arlington, VA.
- M. R. Kessler, "Cyanate Ester Resins with Negative Thermal Expansion Nano-Fillers for Inclusion in Fiber Reinforced Composites" AFOSR 2008 Polymer Chemistry Program Review, May 5-9, 2008. College Park, MD.

Conference Proceedings

- P. Badrinarayanan and M. R. Kessler "Cyanate Ester Nanocomposites with Enhanced Dimensional Stability" Proceedings of the Joint American Society for Composites and Canadian Association for Composite Structures and Materials Conference, September 15-17, 2009. Newark, DE. **Invited**.
- P. Badrinarayanan and M. R. Kessler "Bisphenol E Cyanate Ester Nanocomposites with Low Coefficient of Thermal Expansion" Proceedings of the 67th Annual Technical Conference for the Society of Plastics Engineers, June 22-24, 2009. Chicago, IL. CD-ROM. Pages: 5.
- P. Badrinarayanan, B. Mac Murray, and M. R. Kessler "Thermal and Mechanical Characterization of Bisphenol E Cyanate Ester Nanocomposites" Proceedings of the North American Thermal Analysis Society Annual Conference (NATAS 2008). Aug. 18-20, 2008. Atlanta, GA. CD-ROM, Paper 69: 1-9.
- J. Leonard, Prashanth Badrinarayanan, and Michael R. Kessler "Carbon Nanotube Reinforced Bisphenol E Cyanate Ester Nanocomposites" Great Midwestern Regional Space Grant Consortia Meeting, Sept. 24-25, NASA Glenn Research Center, Cleveland, OH.

CHAPTER 1:   Introduction

1.1 Project Motivation

Fiber-reinforced polymer-matrix composites (PMCs) are used in a wide variety of applications ranging from microelectronics to aerospace structures. Often, high-temperature polymer matrix composites are reinforced with continuous carbon-fibers. The thermal expansion mismatch between the carbon-fiber reinforcement and the polymer matrix is severe and causes significant thermal stresses in the matrix when temperatures fluctuate. The thermal expansion mismatch also results in substantial residual stresses during cure which may lead to significant part warpage and matrix microcracking. This report describes the development and design of a new class of low viscosity resins reinforced with multiwalled carbon nanotubes and nano-particulate zirconium tungstate as a polymer matrix for advanced composites. The novel nanocomposite systems have been used to develop unique hybrid macro-nano composites, which incorporate conventional continuous carbon fibers and nanoparticles, in order to facilitate a reduction in residual thermal stresses due to CTE mismatch between the carbon fiber and the matrix.

1.2 Nanocomposites for Thermal and Mechanical Property Enhancement

The incorporation of discrete nanometer sized particles into polymeric resins has potential to provide value-added properties not present in the neat resin by substantially increasing the functionality and improving the thermal-mechanical properties of the matrix, all without sacrificing the resin's inherent processability. The field of polymer nanocomposites has seen exponential growth over the last ten years, with a plurality of nanoparticles (including layered silicates and carbon nanotubes), polymeric resins, and applications. Unlike traditional "macrocomposites," nanocomposites have extensive interfacial area per volume of reinforcement, which limits the reinforcement to low volume fractions. Consequently, the mechanical properties achieved in the best nanocomposites are much lower than conventional fiber reinforced composites with a high fiber volume fraction. The very short distances between particles (10-50 nm at 1-8 vol%) in nanocomposites results in a comparable size scale between 1) the rigid nanoparticles, 2) the distance between the particles, and 3) the relaxation volume of polymer chain segments, which can result in property enhancements not possible in conventional composite designs.   One key processing obstacle for nanocomposites is the dispersion of nanoparticles throughout the matrix [1,2]. Homogeneous dispersion is complicated because the large surface areas induce attractive forces between the nanoparticles themselves, leading to undesirable, excessive agglomeration. These agglomerations can be very difficult to separate and infiltrate with the matrix [3]. Because of the difficulty in nanoparticle dispersion and the large interphase and interface regions found in nanocomposites, the surface chemistry of the nanoparticles with the host matrix is critical in characterization, processing, and design. In this work, we investigate two systems of nanoparticles: multiwalled carbon nanotubes(CNTs) and nano-sized ZrW_2O_8 as a modifier to a low viscosity cyanate ester resin. A brief description of both the cyanate ester matrix used for nanocomposite development and the nanoparticles such as CNTs and ZrW_2O_8 are provided in the subsequent paragraphs.

1.3 Low viscosity Bisphenol E Cyanate Ester Polymer Matrix

In order for a high-temperature polymer to be suitable in a nano-macro composite, the pre-polymer (monomer) should have a low viscosity at processing temperatures to allow mixing of the nanoparticles and subsequent wetting of the fiber reinforcement. In general, polymers with higher T_g's in the cured state tend to have higher viscosities. Figure 1.1 shows the correlation between the cured state T_g and the temperature at which the uncured thermoset prepolymer has a viscosity of 150 cP [4]. Polyimides are not shown in Figure 1.1 because their lowest melt viscosities are higher than 150 cP.

From Figure 1.1, the one exception to the trend that a higher T_g corresponds to a higher viscosity is a unique type of cyanate ester monomer called bis(4-cyanatophenyl)-1,1-ethane (or bisphenol E cyanate ester) [4-5]. A standard bisphenol A cyanate ester has a melting point of 82°C, but the bisphenol E dicyanate has excellent processing capabilities even at low temperatures with an extremely low viscosity of 90 to 120 cP at room temperature [4-5]. This general relative trend is applicable at higher temperatures as well, with the viscosity of the bisphenol E cyanate ester (BECy) based prepolymers continuing to decrease with increasing temperature. The result is that at virtually all processing temperatures, the BECy system has substantially lower viscosity than other high temperature polymers. These processing characteristics make BECy based resin an excellent candidate for high-temperature polymer matrix nano-macro composites.
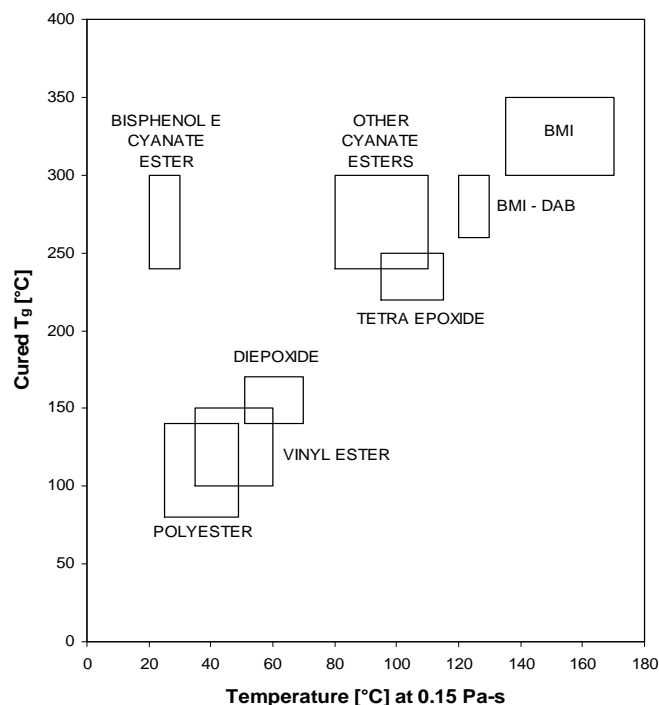

Fig. 1.1. Cured T_g vs. 150 cP Temp.

In general, cyanate esters, correctly named polycyanurates in the polymer form, are characterized by monomers containing reactive ring-forming cyanate functional groups (-O-C≡N). Cyanate esters are a relatively new class of thermosetting polymers that have become a popular replacement for other thermosets in the aerospace and microelectronics sectors because they possess a good combination of high temperature stability and excellent mechanical properties. While cyanate esters are not capable of withstanding as high of temperatures as bismaleimides, they are capable of withstanding extreme temperature variations, which is a significant improvement over epoxies. Also, cyanate esters have excellent adhesive properties and are more resistant to moisture absorption than other thermosets [6]. Finally, cyanate esters have become the resin of choice in many space applications because they have been shown to be less susceptible to matrix microcracking during thermal cycling than BMI and epoxy systems [7]. In addition to their desirable properties in the cured state, cyanate ester resins have excellent wetting characteristics and can be processed using a variety of methods, including resin transfer molding (RTM), filament winding, hand lay-up, and composite prepregs [8]. Like epoxies,

cyanate esters have low toxicity, which makes them much less hazardous than polyimides and bismaleimides [4,9].

1.4   Multi-walled carbon nanotubes

Multi-walled carbon nanotubes [10] and single-walled carbon nanotubes [11,12] are now nearly 15 years old. Since their discovery and synthesis a decade and a half ago, much interest has been shown by researchers and business leaders within the polymer and composites community. The high strength (~30 GPa) and elastic modulus (~1 TPa) [13], and low CTE (α_{axial} ~ -1.5×10^{-6} K^{-1}, $\alpha_{transverse}$ ~ -0.15×10^{-6} K^{-1}) [14] combined with the high aspect ratio of the nanotubes make them ideal candidates for nano-reinforcement in polymer matrix composites. Because of the extremely high strength of the individual nanotubes, failure of nanocomposites nearly always occurs at the interface between the matrix and the nanotubes, and adequate dispersion in the host matrix can be an issue during processing. However, when these obstacles can be overcome (such as by chemical functionalization of the nanotube surface), the benefits of adding CNTs to polymers include increased dimensional stability, conductivity, improved thermal properties, such as T_g and flame resistance, improved mechanical properties (strength and stiffness), and significantly reduced thermal expansion coefficients [15] even at relatively low loading levels.

Researchers have recently investigated the reinforcement of epoxy and polyimide thermosets with CNTs with very promising results for thermal and mechanical property enhancement [16,17]. Recent finite element prediction for CNTs in a polymer matrix indicate that CNTs prove to be much more effective in reducing the overall effective CTE than conventional carbon fibers at the same loading [14]. For example, an epoxy with 0.75 vol% aligned CNTs reveal a longitudinal CTE that is 67% lower than the neat epoxy [14]. Experimental results for unaligned CNTs in epoxy resulted in a 31.5% decrease in CTE at 1 wt. % [18]. However, there has been very little work done on the reinforcement of cyanate ester resins with CNTs. The effects of multiwalled carbon nanotube loading and surface functionality on the thermal, mechanical, and the cure behavior of the low viscosity BECy resin are discussed in Chapter 2 of this report.

1.5   Zirconium Tungstate

While CNTs are one of the most popular nano-reinforcements employed in nanocomposites, zirconium tungstate, ZrW_2O_8, in the nanoparticulate form is quite novel with very little published to date. Zirconium tungstate is one of a small number of materials that exhibit isotropic negative thermal expansion, and its behavior is unique because it has such a strongly negative coefficient of thermal expansion (CTE) over a very wide temperature range (CTE between -8.7 x 10^{-6} K^{-1} and -4.9 x 10^{-6} K^{-1} from 20 to 950 K) [19]. This ceramic material has shown potential for significant reduction of the CTE of composite materials with polymer matrices, though nearly all of the work has focused on micron-sized fillers [20-222326].   The effect of micron size ZrW_2O_8 filler the thermomechanical properties and cure behavior of BECy resin is discussed in Chapter 4 of this report. In addition, details of a surface functionalization strategy to enhance the compatibility between the ceramic oxide particles and the cyanate ester matrix are also elaborated.

The potential for development of polymer nanocomposites through incorporation of zirconium tungstate nanoparticles in a polymer matrix has not received extensive attention, with

only one prior study [22] being reported in the literature. Sullivan and coworkers[22] developed ZrW_2O_8/polyimide thin film nanocomposites with low values of CTE by synthesizing ZrW_2O_8 nanoparticles through a combination of sol-gel processing and reverse micelle methods. Schnabel and coworkers [27] reported loss of nanostructure and particle agglomeration when the ZrW_2O_8 nanoparticles were dried following synthesis by the sol-gel/reverse micelle approach. Furthermore, the sol-gel based methods for synthesis of ZrW_2O_8 have also been reported to result in small amounts of tungsten oxide impurity [27,28]. Synthesis of pure and non-agglomerated nanoparticles is highly desirable for utilizing ZrW_2O_8 as a filler for polymer nanocomposites. Hydrothermal methods which involve acid digestion of precursors at high temperatures and pressures have been reported to result in highly crystalline, pure ZrW_2O_8 nanoparticles. Xing and coworkers [29] reported a hydrothermal method for synthesis of ZrW_2O_8 nanorods by addition of inorganic reactants to hydrochloric acid in a high pressure reaction vessel. The particle width was found to increase from 40 nm to 500 nm, with increasing acid concentration from 10 N to 5 N. The most detailed studies on the effect of various reaction parameters on the morphology of ZrW_2O_8 nanoparticles have been conducted by Colin and coworkers [30]; they examined the effect of various parameters such as acid type, acid concentration, reaction temperature, and time on the particle size, morphology, and crystallinity of ZrW_2O_8 synthesized by hydrothermal methods.

The synthesis of zirconium tungstate nanoparticles by both sol-gel and hydrothermal methods is discussed in Chapter 4 of this report. In this work, the BECy matrix has been reinforced with the negative CTE ZrW_2O_8 nanoparticles to develop polymer nanocomposites with tailored thermal expansion. Chapter 5 provides a detailed understanding of the effect of the negative CTE nanoparticles loading and functionality on the processing and thermal characteristics of BECy, which is crucial for development of dimensionally stable polymer composites with these materials.

1.6   Hybrid Macro-Nano Composites

The unique BECy/ZrW_2O_8 nanocomposites developed in this work have been used as the matrix for preparation of hybrid macro-nano composites through incorporation of unidirectional carbon fibers. Composites were prepared with both a symmetrical and unsymmetrical layup to study the effect on thermomechanical properties and warpage following the cure. The effect of ZrW_2O_8 nanoparticle loading on the thermal, mechanical, and warpage of the carbon fiber reinforced hybrid composites are discussed in Chapter 6 of this report.

CHAPTER 2: Bisphenol E Cyanate Ester/Multiwalled Carbon Nanotubes Nanocomposites

2.1: Introduction and Background

Multiwalled carbon nanotubes (CNTs) are often employed as fillers in multifunctional polymer composites due to their high aspect ratios, high tensile strength and stiffness, tunable electrical conductivity, high thermal conductivity, damping characteristics, and low coefficient of thermal expansion (CTE) [31]. The benefits of CNT reinforcements on the properties of a wide range of thermosetting and thermoplastics polymers have been examined by several researchers and are described in recent review articles [32-36]. However, only one paper has been published on the effect of nanotube loading on the bulk properties of a cyanate ester resin. In recent work, Wang and coworkers [37] have reported that the impact strength of a bisphenol A dicyanate ester resin increased by almost 50 % upon incorporation of 2 wt. % silane treated CNTs.

It is well known that the final properties of thermosets are greatly influenced by the cure schedule used to transform the resin from a liquid monomer to a crosslinked material. In order to fabricate CNT-based polymer matrix composites with optimized thermal and mechanical properties, a detailed understanding of the effect of the nanotubes on the thermosetting resin cure behavior is also essential. The effect of CNT loading on the cure behavior of epoxy resins have been the subject of several recent papers [38-44] and a review article [45]. However, the effect of nanotube loading on the resin cure properties has been found to vary significantly based on the nature of the resin and the type of functional groups attached to the nanotubes.

Unlike the extensive number of studies on the curing kinetics of epoxy/CNT composites, only two papers have examined the effect of CNT loading on the cure of cyanate ester resins. Tang and coworkers [46] published limited data using differential scanning calorimetry (DSC), which suggested that acid functionalized CNTs catalyzed the cure reaction of a cyanate ester/epoxy blend. In more recent work, Fainleib and coworkers [47] used Fourier transform infrared spectroscopy (FTIR) measurements to characterize the effect of CNTs on the cure reaction of Bisphenol A dicyanate ester and reported a significant increase in the degree of cure (α) during the initial stages of the reaction upon incorporation of up to 0.1 wt. % nanotubes. DSC is a preferred technique to evaluate resin cure kinetics since it facilitates direct monitoring of the change in α as a function of reaction time or temperature. However, prior to this work, detailed DSC studies on the effect of CNT reinforcement and surface functionality on the cure behavior of cyanate esters have not yet been performed.

Although cyanate esters have emerged as an important class of resins for development of high performance composites, very few detailed studies have been performed to examine the potential for development of CNT/cyanate ester nanocomposites. In this work, a detailed picture of the effect of CNTs on the properties of the low viscosity BECy resin during various stages of nanocomposite preparation was developed. Furthermore, the effect of nanotube surface functionality on the observed properties was examined through incorporation of nanotubes with hydroxyl groups (OH CNT) and carboxylic acid groups (COOH CNT) attached to the surface. The effect of CNT loading and type on the viscosity of BECy resin was determined by rheology measurements. Dynamic DSC measurements at various constant heating rates (5 to 20 $^{\circ}$C /min) were used to characterize the effect of CNT type on the exothermic cure reaction of BECy for a filler loading of 0.5 wt . %. The dynamic DSC data was fit with phenomenological reaction models, which also facilitated a comparison of reaction parameters for the cure. The effect of

CNT loading and type on the mechanical properties of the cured BECy matrix was measured through instrumented impact testing. Finally, since the objective of this work tailoring the thermal expansion of BECy, the effect of CNT loading (0.5 wt. % and 1 wt. %) and type on the CTE of fully cured BECy samples was evaluated by thermomechanical analysis (TMA).

2.2. Methodology

2.2.1 Materials

The BECy resin and catalyst used in this work was obtained commercially from Bryte Technologies as EX-1510 and EX510 B, respectively. The multiwalled CNTs were supplied by Cheap Tubes, Inc. (Brattleboro, VT) and were produced by a catalyzed chemical vapor deposition method. Multiwalled CNTs were supplied with an outer diameter of 10-30 nm and length of 10-30 microns. The hydroxyl content of the OH CNT and the carboxylic acid content of the COOH CNT were determined by the supplier to be 3.06 wt. % and 2.0 wt. %, respectively, based on a method reported elsewhere [48].

2.2.2 Sample Preparation

BECy/CNT suspensions with 0.5 wt. % and 1 wt. % CNT loading were prepared by dispersing the required amount of nanotubes in BECy by ultrasonic mixing. At 1 wt. % CNT loading, a mixing time of almost 4 hours was necessary to completely disperse the nanotubes in BECy. It is noted that at a loading of 1 wt. %, the OH and COOH functionalized nanotubes were substantially easier to disperse and resulted in a more stable suspension in BECy compared to the unfunctionalized CNTs. Subsequently, 3 phr of catalyst was added to resin and mixed thoroughly. The nanocomposites were degassed under vacuum for 1 hour to eliminate entrapped air. In order to maintain the levels of nanotube dispersion and prevent settling and agglomeration during the cure process, the nanocomposite mixture was cured up to the gel point in an oven with a rotating mounting by isothermal curing at 160 $^{\circ}$C for 45 minutes.   The partially cured nanocomposites were further cured in a programmable convection oven at 180 $^{\circ}$C for 2 hours. A post cure was also performed by heating the samples to 1 $^{\circ}$C /min 250 $^{\circ}$C for 2 hours. The fully cured specimens were machined according to the specifications for each test.

2.2.3 Characterization

Rheological testing was performed for uncured BECy/CNT mixture using an AR2000EX rheometer (TA Instruments) in the continuous mode. Approximately 1 ml of each type of BECy /CNT suspension was injected between two parallel plates using a syringe. The shear rate was increased from 0 to 100 s^{-1} to determine the effect of the nanotube loading and surface functionalization on the viscosity of the resin. For the DSC measurements, suspensions containing 0.5 wt. % of the unfunctionalized CNTs, OH CNTs, and COOH CNTs in BECy resin were prepared without addition of catalyst. Prior to each test, 9-11 mg of sample was transferred to hermetic aluminum pans. The samples were heated from 25 $^{\circ}$C to 375 $^{\circ}$C at heating rates of 15, 10, 7, and 5 $^{\circ}$C/min in a Q2000 DSC (TA Instruments) to examine the effects of the nanotubes on the cure behavior of BECy resin. Transmission electron microscopy (TEM) of the fully cured nanocomposites was performed using a JEOL 2100 200 kV microscope. The samples were prepared for imaging by cutting a thin slice using an ultramicrotome. Scanning electron microscopy (SEM) was performed with the fracture surfaces of the fully cured nanocomposites using a Hitachi S 2460 N microscope. The fracture surfaces were prepared for

imaging by sputter coating with gold under vacuum. The nanocomposite samples for TMA measurements were machined with dimension of 6 x 3 x 3 mm. The tests were conducted by performing a preliminary heating scan at 5 ^{o}C/min to 300 ^{o}C to erase the effect of prior thermal histories. The CTE was measured from a second heating performed at 5 ^{o}C/min after cooling the sample at 5 ^{o}C/min through the glass transition. The impact strength of the fully cured specimens were determined using a Tinius Olsen Charpy impact strength tester. The samples were machined with dimensions of 60 x 6 x 2 mm and a 60° notch. The energy and friction loss in the system was calibrated and verified prior to the measurements by swinging the pendulum for 11 half cycles.

2.3   Results and Discussion

The effect of CNT loading on the viscosity of BECy resin at 23 ^{o}C is compared for shear rates up to 100 s^{-1} in Figure 2.1. The viscosity of BECy is nearly constant (0.08-0.09 Pa.s) over the shear rates examined, thereby approximately exhibiting Newtonian flow behavior. The resin viscosity increases slightly for suspensions with 0.5 wt. % unfunctionalized CNT loading, whereas a more significant increase can be observed for the 1 wt. % system. The viscosity of the CNT/BECy resins are found to decrease with increasing shear rates and exhibit shear thinning behavior, which is found to be more dramatic at 1 wt. % CNT loading. The shear thinning behavior may be attributed to the breaking up of physical entanglements and agglomerates of CNTs at higher shear rates. The effect of CNT functionalization on the rheological behavior is compared in Figure 2.2, for a loading of 1.0 wt. %. The BECy/CNT suspension exhibits the highest viscosity and the most dramatic shear thinning behavior, while the introduction of OH and COOH functional groups results in a lower viscosity at the same loading. A similar trend was also observed for a CNT loading of 0.5 wt. %. The lower viscosity of the nanocomposites with OH and COOH CNTs may be indicative of the presence of lower extents of agglomerates and better dispersion of the nanotubes in BECy as a consequence of surface functionalization.
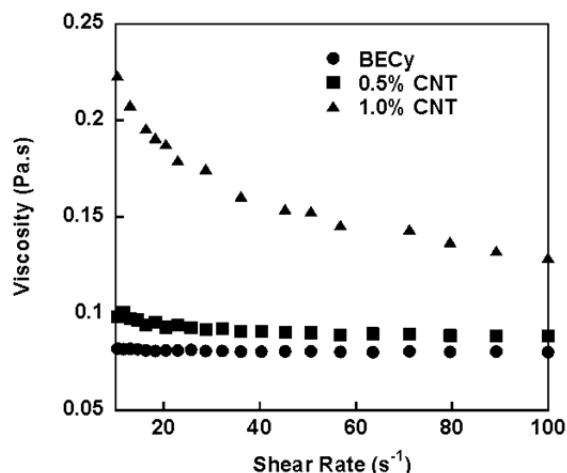
Figure 2.1: Effect of unfunctionalized CNT loading on the viscosity of BECy resin
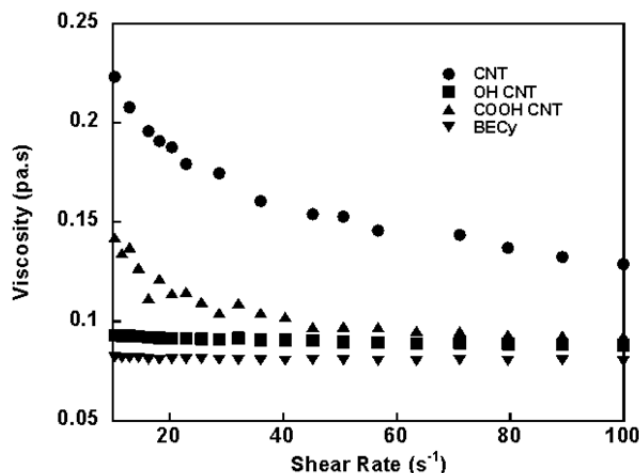
Figure 2.2: Effect of CNT surface functionality on the viscosity of BECy resin at 1.0 wt. % loading

The heat flow curves obtained from dynamic DSC measurements of BECy resin and the nanocomposites with 0.5 wt. % CNT loading are shown in Figure 2.3 a-d. The impact of CNT loading on the cure kinetics of BECy may be characterized in terms of the cure onset and peak temperatures of the reaction exotherms. The exotherm onset temperature (T_o) represents the temperature where the cure is initiated while the exotherm peak temperature (T_p) corresponds to the temperature where almost 50 % of the monomer is converted to crosslinked polymer. The onset and peak temperatures obtained from Figure 2.3a-d for BECy and BECy/CNT resins are compared in Figure 2.4 and 2.5, as a function of the heating rate and CNT functionality. The onset and peak temperatures shift to higher temperatures with increasing heating rate, as expected.

Incorporation of pristine CNTs results in a 12-14 ^{o}C decrease in the onset temperature while incorporation of COOH CNTs decreases the onset temperature by 14-18 ^{o}C. On the other hand, upon incorporation of OH CNTs the values of T_o exhibit a dramatic decrease and are found to be 40-55 ^{o}C lower than the values of T_o for BECy, depending on the rate. The average decrease in the T_p of the cure exotherm is found to be 7.2 and 9.7 ^{o}C for BECy upon incorporation of pristine CNT and COOH CNT, respectively. However, the value of T_p decreases by almost 25 ^{o}C upon incorporation of OH CNT. The observed decrease in T_o and T_p of the cure exotherm for all three types of CNTs is indicative of a catalytic effect as a consequence of nanotube loading. The catalytic effect is most pronounced for OH CNT loading, which results in the largest decrease in the values of T_o and T_p.   In this case, the presence of the hydroxyl groups on the nanotubes may promote covalent bond formation between the cyanate ester resin and the filler; this can lead to early reaction initiation and an increase in cure rate **Error! Bookmark not defined.**, which explains the dramatic catalytic effect observed for the OH CNTs. However, this effect appears markedly reduced for COOH CNTs which results in a smaller decrease in values of T_o and T_p when compared to OH CNTs. The least catalytic effect is observed in the case of the unfunctionalized CNTs.

The effect of the nanotubes on BECy cure kinetics may be further characterized using phenomenological reaction models. The degree of cure (α) during the dynamic DSC measurements may be estimated as shown in Equation 2.1 below:

$$\alpha(t) = \frac{H(t)}{H_R} \qquad (2.1)$$

where $H(t)$ is enthalpy of the reaction at time t and H_R is the total enthalpy of the reaction obtained by integration of the area under the reaction exotherm. Phenomenological models can be used to fit dynamic DSC measurements by describing the reaction rate as a function of the conversion, α, and a temperature dependent rate constant, as shown in Equation 2.2:

$$\frac{d\alpha}{dt} = f(\alpha)\, K(T) \qquad (2.2)$$

Substituting the Arrhenius expression for rate constant $K(T) = A\exp\left(\dfrac{-E_a}{RT}\right)$,where E_a is the activation energy for the reaction, and the heating rate, $\beta = dT/dt$, gives the rate of cure with respect to temperature, as shown by Equation (2.3).
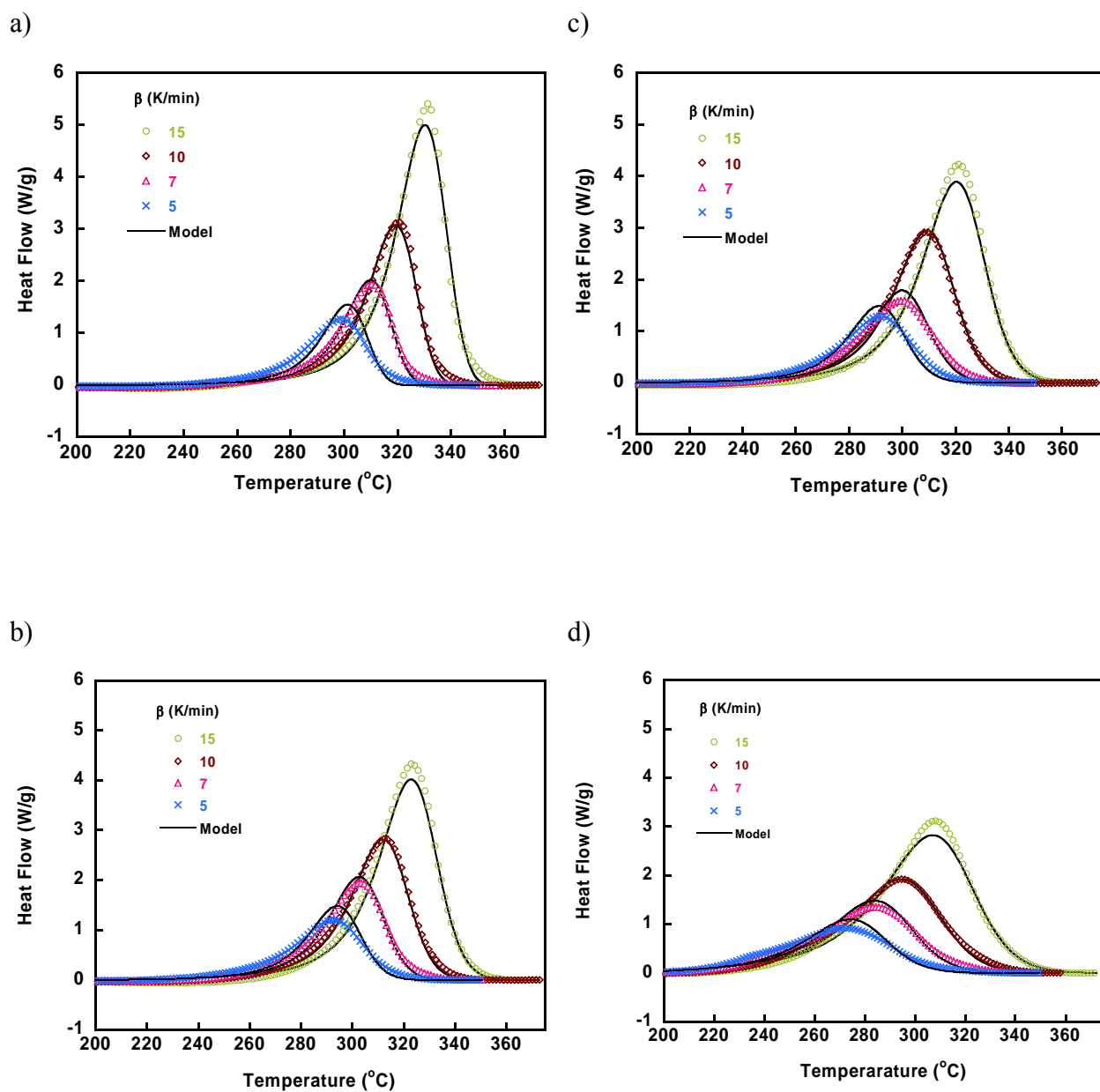
Figure 2.3: Heat flow curves obtained from dynamic DSC measurements of CNT/BECy nanocomposites a) neat BECy b) 0.5 wt. % CNT/BECy c) 0.5 wt. % COOH CNT/BECy d) 0.5 wt. % OH CNT/BECy. The symbols are data points obtained from experiments. The solid lines are best fits from autocatalytic model (type 1).
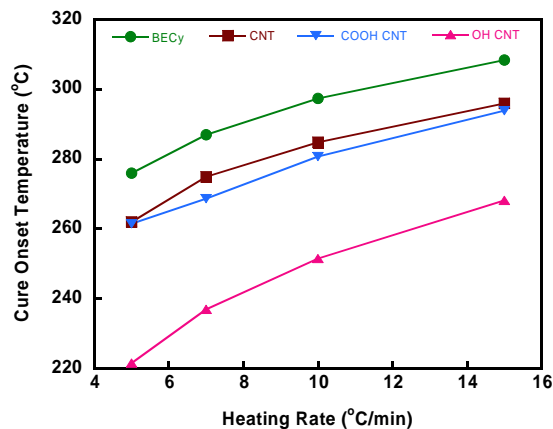
Figure 2.4: Effect of CNT surface functionality on the onset temperature of BECy cure exotherm for 0.5 wt. % loading as a function of the heating rate. The lines are drawn as a visual guide.
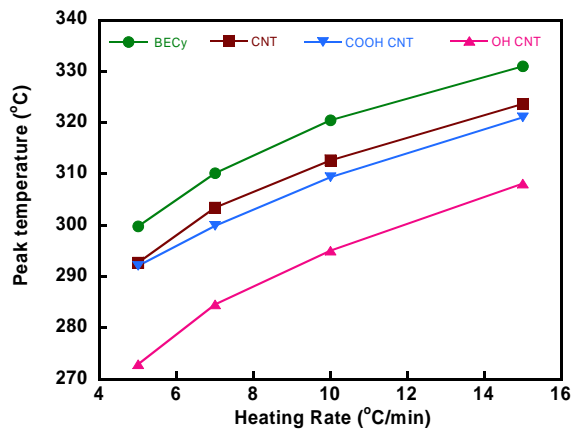
Figure 2.5: Effect of CNT surface functionality on the peak temperature of BECy cure exotherm for 0.5 wt. % loading as a function of the heating rate. The lines are drawn as a visual guide.

$$\frac{d\alpha}{dT} = \frac{A}{\beta} \exp\left(\frac{-E_a}{RT}\right) f(\alpha) \tag{2.3}$$

In this work, the ability of an nth order model and two simple autocatalytic models (shown in Table 1) in describing the dynamic DSC measurements were examined. The data obtained at four rates from 15 ^{o}C/min to 5 ^{o}C/min for each system was fit simultaneously with the models shown in Table 1 in order to determine the best fit model. As shown in Table 2.1, for all systems examined, the lowest F-value and the best description of the dynamic DSC measurements were obtained with the autocatalytic model (Type 1). The solid lines in Figures 2.3 a-d represent the model calculations and are found to be in good agreement with the experimental data for all the nanocomposites.

Table 2.1: Phenomenological Reaction models used in this work. The F-value determines the quality of the fit with F-value of 1.0 representing the best fit.

| Model Type	f(α)	Fitting Parameters	F-Value			
			BECy	**CNT**	**OH CNT**	**COOH CNT**
nth order	$(1-\alpha)^n$	A, E_a, n	15.5	8.8	3.5	8.7
Autocatalytic (Type 1)	$(1-\alpha)^n(1+K_{cat}\alpha)$	A, E_a, n, K_{cat}	1.0	1.0	1.0	1.0
Autocatalytic (Type 2)	$(1-\alpha)^n\alpha^m$	A, E_a, n, m	1.6	1.2	1.2	1.1

The model parameters obtained upon fitting the DSC measurements with the best fit autocatalytic model are tabulated in Table 2.2. The trend for the values of E_a is found to be BECy>CNT>COOH CNT>OH CNT. Hence, incorporation of OH CNTs results in the most dramatic catalytic effect and as a consequence, leads to a significant decrease in the activation

energy of the cure. The reaction order exhibits an inverse correlation with E_a and is found to be lowest in the case of BECy and highest for the system with OH CNTs. The kinetic parameters can be used to predict the extent of cure under isothermal conditions at any cure temperature and may be used for optimization of the resin cure schedules upon incorporation of CNTs.

Table 2.2: Model parameters obtained from a simultaneous fit of the dynamic DSC data for each system with autocatalytic model (Type 1).

| Sample	Log (A/s^{-1})	E_a (kJ/mol)	n	Log K_{cat}
BECy	5.6	100.09	0.88	1.53
CNT	5.8	98.09	1.02	1.32
COOH CNT	5.6	96.06	1.07	1.33
OH CNT	4.56	79.37	1.11	0.85

The TEM images of the nanocomposites with 1 wt. % CNT loading after full cure are shown in Figure 2.6a through c. The images do not reveal significant differences between the three types of nanocomposites in this work. At lower magnifications the images are characterized by the presence of CNT rich regions with clusters of nanotubes and CNT poor regions, for all three systems examined in this work. However, a slightly more heterogeneous distribution with more broken nanotubes is observed in the case of the pristine CNTs perhaps due to the longer duration of ultrasonic mixing compared to the functionalized nanotubes.
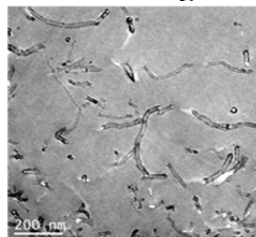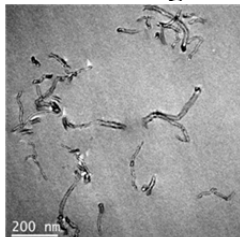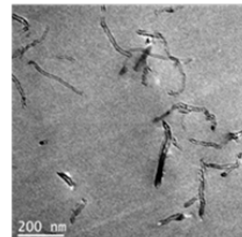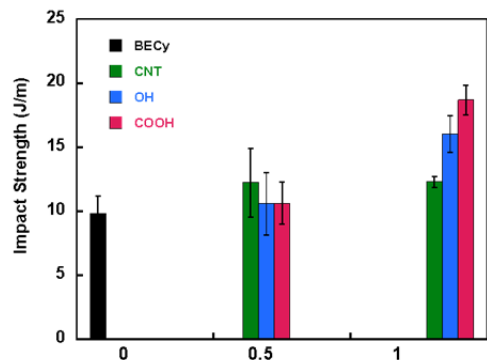

a)   b)   c)

Figure 2.6: TEM images of BECy nanocomposites with 1 wt. % a) non functionalized CNTs b) COOH CNTs c) OH CNTs

Figure 2.7: Effect of CNT type and loading on the impact strength of fully cured BECy

The impact strength of the fully cured BECy/CNT nanocomposites is plotted as a function of filler loading and type in Figure 2.7. The error bars are standard errors based on three measurements for each system. Incorporation of pristine CNTs results in a 25 % increase in impact strength at both 0.5 wt. % and 1 wt. % loading. However, for the other two types of composites, the impact strength is found to increase with increasing filler loading. At 1 wt. % loading, the impact strength of the OH CNT/ BECy nanocomposite is found to be 63 % higher than BECy. Similarly, the impact strength of the COOH CNT/BECy nanocomposite is

found to be 91 % higher than BECy. The impact strength in polymer nanocomposites may be influenced by factors such as filler dispersion, interface between filler and matrix, and extent of energy absorption by the filler [49]. The significantly higher values of impact strength at 1 wt. % loading for the OH CNTs and COOH CNTs may be due to the formation of covalent bonds between the nanotubes and polymer matrix during the cure process [50]. The functional groups also improve the surface compatibility between the polymer matrix and the nanotubes and the catalytic effect exerted by the functional groups could lead to changes in the crosslinked network that contribute to the observed improvements in impact strength.

The fracture surface images from SEM of the fully cured BECy resin and the nanocomposites are shown in Figure 2.8 a-d. The fracture surface morphology of the neat BECy resin is characterized by the presence of step like striations, which is characteristic of brittle failure, as shown in Figure 2.8a. On the other hand, the nanocomposites are characterized by crevices and plate-like patterns as shown in Figure 2.8b -d. Such patterns are more enhanced in the case of OH CNT and COOH CNT nanocomposites (2.8c and d) and facilitate absorption of more fracture energy [49,50]. Another feature in the images for the nanocomposites with OH and COOH CNTs are the existence of cracks, which exhibit significant changes in direction of propagation. Wetzel and coworkers [49] indicated that the presence of well dispersed nanoparticles may facilitate such crack deviation mechanisms that lead to enhancements in impact strength while presence of agglomerates lead to an overall decrease in impact strength. The fact that the impact strength of BECy is not decreased for all three types of nanotubes is indicative of achievement of reasonable extent of dispersion in this work.


a)

b)

c)

d)
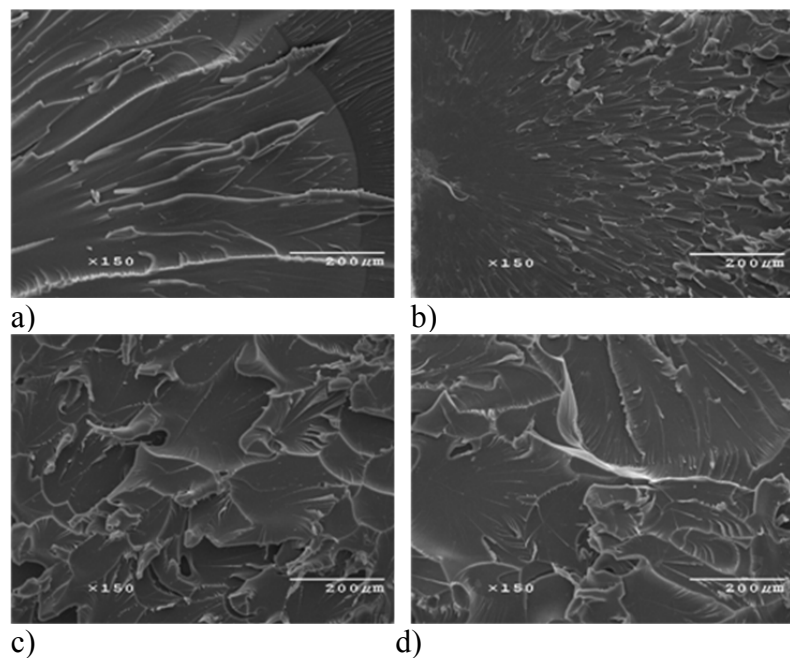
Figure 2.8: SEM images of CNT/BECy nanocomposites a) neat BECy b) 1.0 wt. % CNT/BECy c) 1.0 wt. % COOH CNT/BECy   d) 1.0 wt. % OH CNT/BECy.

TMA was used to determine the T_g of the nanocomposites from dimension change data as the point of intersection of glassy and liquid lines drawn from regions above and below the glass transition, respectively. The relationship between T_g and filler loading are plotted for the three types of nanotubes in Figure 2.9. At any given loading, nanocomposites with functionalized nanotubes exhibit higher values of T_g with the COOH CNTs resulting in the highest values. At 0.5 wt. % loading, T_g of BECy increases by 2 and 4 °C, upon incorporation of OH and COOH CNTs, respectively. For a nanotube loading of 1 wt. %, the T_g of BECy decreases by almost 8 °C upon incorporation of

Figure 2.9 Effect of CNT type and loading on the glass transition temperature of fully cured BECy nanocomposites.

unfunctionalized CNTs. However, the magnitude of reduction is substantially lowered upon incorporation of COOH CNTs and is found to decrease by approximately 2 °C. The enhancement in T_g at 0.5 wt. % loading may be attributed to a decrease in mobility of the polymer chains due to the presence of well dispersed nanotubes [51]. At 1 wt. % loading, any enhancement may be offset due to limitations imposed by the presence of nanotubes on the formation of a crosslinked network [52], which is found to be more dramatic for unfunctionalized CNTs.

The effect of CNT incorporation on the CTE of BECy is also of significant interest since multiwalled CNTs are characterized by low values of CTE [53] and have the potential to enhance the dimensional stability of the polymer matrix. The values of CTE (α_g) of the nanocomposites can be determined from TMA measurements, according to Equation 2.9 below:

$$\alpha_g = \frac{1}{L_0}\frac{dL}{dT}$$

(2.9)

where L_o is the original sample length, dL represents the change in length of the sample with temperature change dT. The values of glassy CTE obtained from the slope of the dimension change curves in the temperature range of 50 -100 °C are tabulated in Table 2.3. In previous work in the literature [54], incorporation of up to 10 wt. % multiwalled nanotubes resulted in a 4 % decrease in the glassy CTE of an epoxy resin. In this work, the maximum decrease in CTE is found to be 2.5 % for 1 wt. % loading. This magnitude of reduction is substantially greater than values expected on the basis of the rule of mixtures. The value of CTE for 1.0 % CNT and 1.0 % OH CNT are similar and approximately 1% lower than the value obtained for 1.0 wt. % COOH CNT. Considering the minimal effect of CNT type and loading on the CTE of BECy, the lack of difference between the three types of CNTs for the low loadings employed in this work is perhaps not unexpected. Further improvements of the thermo mechanical properties of the BECy nanocomposites may be possible through exploration of alternative functionalization strategies and careful optimization of the cure schedules based on the influence of the nanotube type on the resin cure behavior.
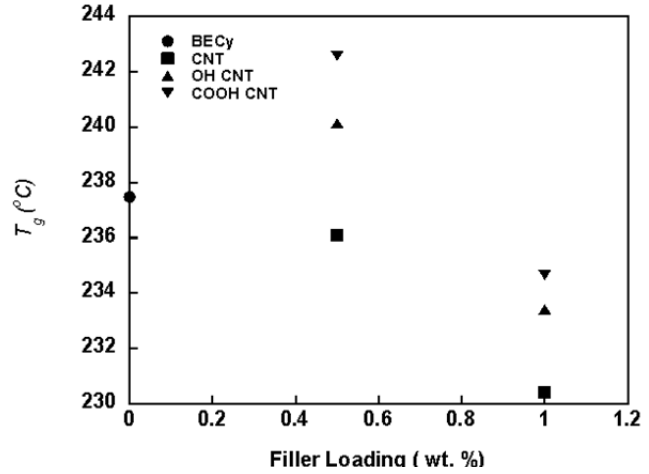
Table 2.3: CTE Values for CNT/BECy nanocomposites.

| Sample	CTE ($\times 10^{-6} \ {}^{\circ}C^{-1}$)
BECy	60.81
BECy/0.5 wt. % CNT	60.89
BECy/0.5 wt. % OH CNT	60.49
BECy/0.5 wt. % COOH CNT	60.69
BECy/1.0 wt. % CNT	59.26
BECy/1.0 wt. % OH CNT	59.32
BECy/1.0 wt. % COOH CNT	60.13

2.5   Conclusions

In this work, the effect of nanotube loading and functionalization on the properties of a unique, cyanate ester resin was examined. Upon incorporation of up to 1 wt. % nanotubes, the resin with the unfunctionalized nanotubes is found to exhibit the highest viscosity and most dramatic shear thinning behavior, possibly due to a lower extent of filler dispersion and presence of more agglomerates in comparison to the suspensions with functionalized nanotubes. The incorporation of CNTs is found to result in a catalytic effect on the cure of BECy resin with OH CNTs exhibiting the most dramatic effects. The dynamic DSC measurements of all the nanocomposites are well described by a simple n^{th} order autocatalytic model. The activation energy determined by model fitting is found to be the lowest for the nanocomposite with OH CNTs, consistent with the dramatic reduction in the onset and peak temperatures observed by DSC.

The impact strength of BECy was increased by 91 % and 63 % upon incorporation of 1 wt. % COOH CNTs and OH CNTs, respectively. SEM images of fracture surfaces for the nanocomposites at 1wt. % loading reveal features in the case of nanocomposites with OH and COOH CNTs, which facilitate absorption of fracture energy and enhance the impact strength. The increase in impact strength is achieved without a significant reduction in T_g, especially upon incorporation of OH an COOH CNTs.   The observed improvements for the functionalized CNTs can be attributed to the ability of the functional groups to form covalent bonds with the matrix during the cure. A small but promising reduction is observed in the CTE of BECy upon incorporation of 1 wt. % CNTs indicating that the dimensional stability can be further enhanced at higher loadings after appropriate surface functionalization of the nanotubes.

CHAPTER 3: BECy/ZrW$_2$O$_8$ Composites-Effect of Filler Loading and Functionalization

3.1   Introduction

The negative CTE behavior observed on heating ZrW$_2$O$_8$ is due to transverse vibration of the interconnecting oxygen atom between zirconium and tungsten atoms in the ZrW$_2$O$_8$ crystal, which leads to rotations of the rigid polyhedra units in the crystal lattice and a decrease in the effective bond lengths [19,,56]. A schematic representation of the ZrW$_2$O$_8$ crystal structure is shown in Figure 3.1. Depending on the temperature and pressure, ZrW$_2$O$_8$ can exist in three different phases which are characterized by different crystal structures. In the α phase, ZrW$_2$O$_8$ possesses a cubic crystal structure and exhibits the most negative CTE values (-8.7 × 10^{-6} ^{o}C^{-1}). Upon heating ZrW$_2$O$_8$ above 150 ^{o}C, the unattached oxygen atoms in the tungsten oxide tetrahedra reorient themselves, which results in a reversible transition from the α phase to the β phase [1]. The β phase is characterized by a disordered crystal structure and can be transformed back to the α phase upon cooling. At pressures above 200 MPa, ZrW$_2$O$_8$ exists in the γ phase which is characterized by an orthorhombic crystal structure and the lowest negative CTE values (-1 × 10^{-6} ^{o}C^{-1});
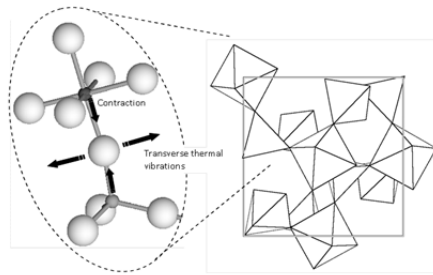

Figure 3.1: A section view of ZrW$_2$O$_8$ crystal structure comprised of zirconium oxide octahedra connected to tungsten oxide tetrahedra through shared oxygen atoms.

In spite of its large negative CTE and interesting phase behavior, only a few researchers have examined the impact of ZrW$_2$O$_8$ as a filler in polymer matrix composites. Shi and coworkers [20] reported that the incorporation of 30 volume (vol.) % of ZrW$_2$O$_8$ with a polyester resin resulted in a 40 % decrease in CTE. Weyer and coworkers [21] observed an 80 % reduction in CTE upon addition of up to 52 vol. % ZrW$_2$O$_8$ in a cyanate ester resin. Sullivan and Lukehart [22] examined the impact of micron size and nano size zirconium tungstate reinforcements on the CTE behavior of a polyimide film; they reported a 30 % decrease in CTE upon incorporation of 22 vol. % micron size ZrW$_2$O$_8$, whereas the CTE was found to decrease by 21 % upon incorporation of only 1.7 vol. % nano size filler. Weyer et al.[21] investigated the reinforcement of a commercial cyanate ester, CTD 403, with ZrW$_2$O$_8$, measuring the CTE's of different cross-sections of cylindrical composite samples in which the filler had settled significantly . Tani and coworkers [26] have reported a 70 % decrease in CTE upon incorporation of 52 vol. % zirconium tungstate in a phenolic resin. In more recent work, Miller and coworkers [25] have reported up to 50 % reduction in CTE of an epoxy resin upon incorporation of 40 vol. % ZrW$_2$O$_8$ filler. The dramatic reductions in CTE achieved through incorporation of ZrW$_2$O$_8$ can greatly improve dimensional stability of polymers, which is often a limitation with conventional polymer matrix composites.

In this work, the direct incorporation of micron size ZrW$_2$O$_8$ in BECy resin was accomplished using ultrasonic mixing and by curing the BECy/ ZrW$_2$O$_8$ mixture in a custom built rotating oven, to prevent settling during cure. The filler content in the test specimen are verified by thermogravimetric analysis (TGA). The effect of negative CTE filler loading on the overall thermal expansion of the cured composite was examined by thermomechanical analysis

(TMA). The reductions in CTE observed in the experiments are compared against predictions from various theoretical models for CTE. TMA measurements were also used to examine the effect of filler loading on the glass transition temperature (T_g) of the composites. The chemical structures of BECy monomer and a unit of the crosslinked network obtained after curing are represented in Figure 3.2. Most methods for synthesis of ZrW_2O_8 result in hydroxyl (OH) groups at the particle surface [25], which are expected to catalyze the cure of BECy. The thermomechanical properties of a composite are significantly influenced by the resin cure conditions; hence, a detailed understanding of the effect of ZrW_2O_8 filler loading on the cure of BECy resin is crucial to optimize the properties of a high performance thermoset and the cure schedules. Hence, this work examines for the first time, the effect of ZrW_2O_8 filler loading on the cure kinetics of a BECy resin by differential scanning calorimetry (DSC) measurements. Furthermore, since some studies [22] in the literature have reported that significant improvements in thermomechanical properties of thermoset resins are possible through surface treatment of ZrW_2O_8, the impact of a silane surface treatment of ZrW_2O_8 on the T_g and cure behavior of BECy composites was also studied.
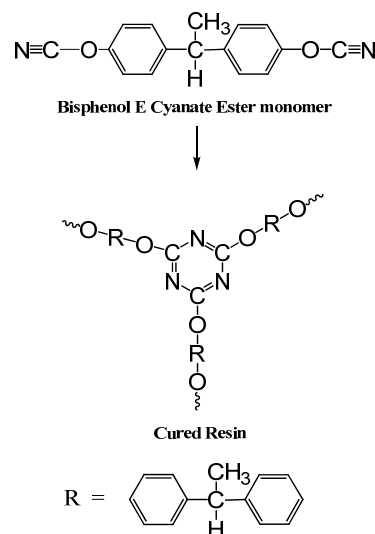
Figure 3.2: Cyclotrimerization reaction of bisphenol E cyanate ester (BECy).

3.2 Methodology

3.2.1 Materials

The Bisphenol E cyanate ester used in this study was purchased from Bryte technologies (Morgan Hill, CA) as EX-1510 resin. The resin was cured by adding three parts of catalyst (EX-1510 B) obtained from Bryte technologies per 100 parts of resin. The ZrW_2O_8 used in this study was obtained from ATI Wah Chang (Albany, OR). The zirconium tungstate powder was dried at 120 ^{o}C for 1 hour to remove moisture prior to mixing with resin.

3.2.2 Sample Preparation

Loadings of 10, 20, and 65 vol. % micron sized zirconium tungstate filler was incorporated in BECy resin under shear mixing. The filler loading of 65 vol. % was chosen based on model calculations as the upper limit of ZrW_2O_8 loading for which the BECy composite approaches zero CTE. The resin-filler mixtures were sonicated for c.a. 3 hours in a Branson ultrasonic water bath (Model 1510, 60 Hz, 155 W) to fully disperse the particles in the resin. The dispersed mixtures were transferred to a mold and the samples were degassed for 1 hour. For the lower filler loadings (10-20 vol. %), the samples were cured up to the gel point in a rotating oven at 130 ^{o}C to prevent settling of the fillers during cure. The final cure was performed in a convection oven at a programmed rate (ramp to 180 ^{o}C at 1 ^{o}C/min, soak for 2 hours, ramp to 250 ^{o}C at 1 ^{o}C/min , soak for 2 hours). The composite with 65 vol % zirconium tungstate was cured at 180 ^{o}C by compression molding in a hot press and then post cured in the convection oven at 250 ^{o}C for 2 hours. The samples were subsequently cooled to room temperature and machined according to the specifications of the experiments

### 3.2.3 Silane treatment of ZrW$_2$O$_8$

Zirconium tungstate particles were dispersed with 125 ml of distilled and dry tetrahydrofuran (THF) in a 250 ml flask by sonication in an ultrasonic bath (Branson Model 1510). Next, 2.5 ml of Glycidyloxypropyl trimethoxysilane (GPS) solution was injected in to the flask and the mixture was refluxed for 2 days at 95 ^{o}C. The solution was centrifuged to separate the functionalized particles from the mixture. The functionalized ZrW$_2$O$_8$ (F-ZrW$_2$O$_8$) particles were washed with THF to remove excess GPS and separated from the solution by centrifugation. The particles were allowed to dry at room temperature for 2 days and subsequently dried under vacuum to remove residual solvents.

3.2.4 Characterization

The CTE of the composites were measured using a Q400 thermomechanical analyzer from TA Instruments. The measurements were performed using a specimen with dimensions of $6 \times 3 \times 2$ mm. The measurements were performed by heating the sample at the rate of 5 ^{o}C/min from room temperature to 300 ^{o}C. A second heating scan was performed at 5 ^{o}C/min after cooling the sample through the glass transition at a rate of 5 ^{o}C/min. The value of T_g was measured as the onset point in the dimension change curve versus temperature of the second heating scan. The dynamic storage modulus of the composites was determined as a function of filler loading using a Q800 dynamic mechanical analyzer from TA instruments. The measurements were performed using a specimen with dimensions $15 \times 3 \times 2$ mm. The measurements were performed in the three point bending mode at a frequency of 1 Hz, amplitude of 10 μm, and a pre load force of 0.1 N. The storage modulus was determined as a function of temperature for each fully cured composite specimen by heating at a constant rate of 3 ^{o}C/min. The weight percent of filler loading in the test specimen were ascertained using a Q50 thermogravimetric analyzer from TA Instruments. The tests were performed by heating a small quantity of the composite specimen at 20 ^{o}C/min up to 800 ^{o}C in the presence of air. Cure characterization of the BECy/ZrW$_2$O$_8$ BECy/ F-ZrW$_2$O$_8$ composites was performed in a model Q20 DSC from TA Instruments . T-Zero hermetic pans (TA Instruments) were loaded with c.a. 8 mg samples and cured at 5, 7, 10, and 15 K/min heating rates from room temperature to 350 ^{o}C or 360 ^{o}C.

3.3 Results and Discussion

The heat flow curves obtained from DSC measurements of the fully cured composites at a heating rate of 10 ^{o}C/min are shown in Figure 3.3. The heat flow curves for all three samples indicate a γ-α transition suggesting that the ZrW$_2$O$_8$ filler in the cured composites is in the γ phase. However, the α-β phase transition is not clearly evident in the heat flow signals for any of the composites in Figure 3.3. Heating beyond the expected temperature range of the α-β transition leads to glass transition of the composite and is characterized by a step change in the heat flow signal. The intensity and width of the γ-α transition depends on the ZrW$_2$O$_8$ loading,
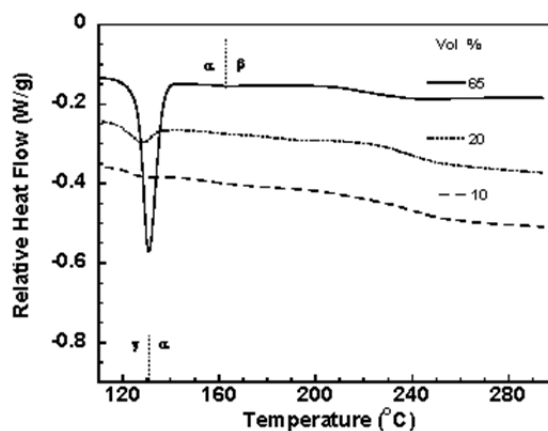

Figure 3.3: Heat flow measurements of BECy/ZrW$_2$O$_8$ composites for various filler loadings. The y-axis is shifted for comparison.

leading to slight changes in the transition peak temperatures as shown in Figure 3.3. The ZrW_2O_8 in the cured composites was expected to be in the α phase due to the high temperatures employed in the cure. However, it is possible that the compressive stresses during the formation of the crosslinked polymer network might be sufficient to induce the formation of the γ phase in ZrW_2O_8; this is further verified in Figure 3.4, where the endotherm corresponding to the γ-α transition is observed in the heat flow curve prior to the cure exotherm of BECy reinforced with 10 vol. % ZrW_2O_8. Upon performing a second heating scan following the cure, another endotherm corresponding to the γ-α transition is observed which is followed by the glass transition of the fully cured composite. This demonstrates that even though the γ-α transition occurred prior to the cure, the γ phase was induced in the cure process leading to the γ-α transition in the second heating scan. As expected, a third heating scan of the fully cured composite does not exhibit the γ-α transition, as evident from the comparison in the inset of Figure 3.4.
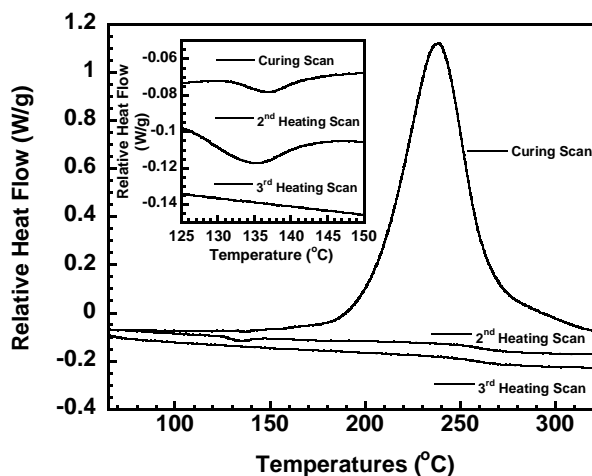

Figure 3.4: Heat flow measurements of BECy/ 10 vol. % ZrW_2O_8 composites. The first scan is a heating run to cure the resin. The second and third scans are performed for fully cured composites. As shown in the inset, the first and second scans exhibit an endothermic γ-α phase transition peak.

The weight loss curves obtained upon heating the composites at 20 °C/min in a TGA are shown in Figure 3.5. BECy degrades completely at temperatures above 750 °C and the remaining wt. % indicates the ZrW_2O_8 content in the composites. Upon determining the wt. % of ZrW_2O_8 in 3-5 specimens from different section of each composite sample, the maximum standard deviation of the wt. % was found to be 1.1 wt. % (or 0.26 vol. %) indicating that the filler was reasonably well dispersed in the resin.
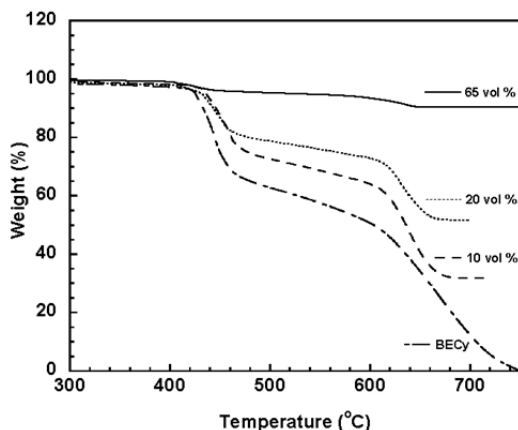
Figure 3.5: Comparison of TGA measurements for BECy and BECy/ZrW_2O_8 composites.
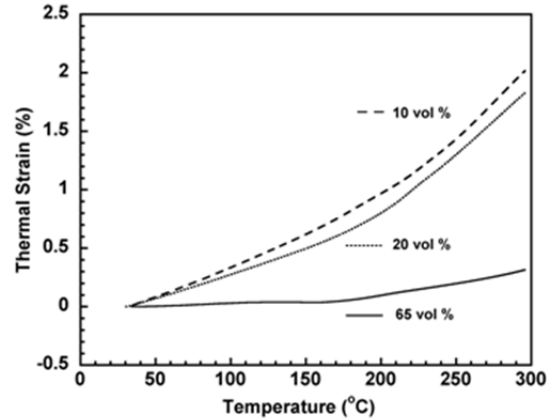
The thermal strains versus temperature from TMA measurements for BECy resin is shown in Figure 3.6. The first heating scan at 5 °C/min is performed to erase the previous thermal history of the specimen. The second heating curve exhibits a change in slope due to the onset of the glass transition of the composite; the value of T_g can be determined from the point of intersection of tangents drawn from above and below the glass transition temperature range, as shown in Figure 3.6. Below T_g the thermoset is in a glassy state, whereas above T_g it exists in a rubbery state. The CTE in the glassy and rubbery state can be determined from the slope of the dimension change curves, as shown in Figure 3.6. The second heating responses of all three composites with various loadings of ZrW_2O_8 are compared in Figure 3.7. The magnitude of thermal strain is found to decrease with increasing ZrW_2O_8 loading. The thermal strain is found to be less than 0.05 % for the composite with 65 vol. % $ZrW_2O_8,$ prior to the onset of the glass transition.
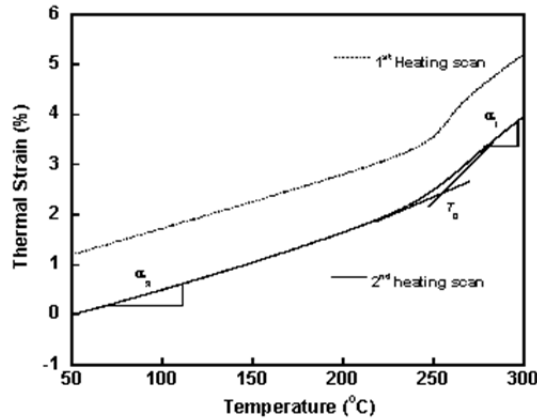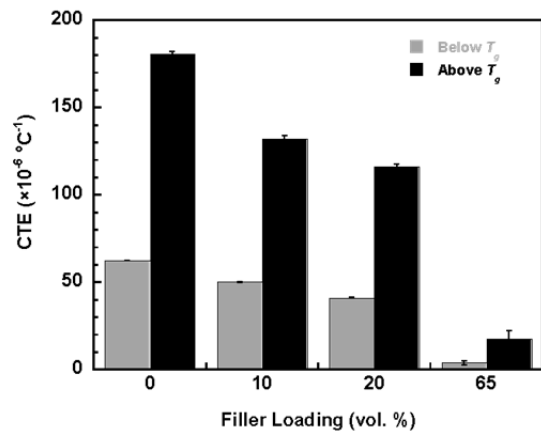

Figure 3.6: Thermal strain curves obtained from TMA measurements for BECy. The second heating curve was obtained after cooling through the glass transition at 5 K/min.

Figure 3.7: Comparison of thermal strain curves obtained from second heating runs in TMA measurements for various filler loadings.

The values of CTE at temperatures above and below the glass transition temperature are compared as a function of ZrW_2O_8 loading in Figure 3.8. Unlike other materials such as multiwalled carbon nanotubes, which have been reported to decrease the CTE only at temperatures below T_g of the polymer matrix [57], the large negative CTE of ZrW_2O_8 over a wide temperature range ensures a decrease in CTE above and below the glass transition temperatures. Upon increasing the ZrW_2O_8 loading to 65 vol. %, the CTE of the composite at temperatures below T_g is found to be 92 % lower than the CTE of the neat resin; similarly, the CTE of the composite with 65 vol. % ZrW_2O_8 loading is found to be 88 % lower than the neat resin, at temperatures above T_g.

Figure 3.8: Comparison of CTE values at temperatures above and below the glass transition

Micromechanical models of CTE can be used to predict the change in CTE of a composite upon incorporation of fillers [58-60], as shown in Figure 3.9. Typically, the three
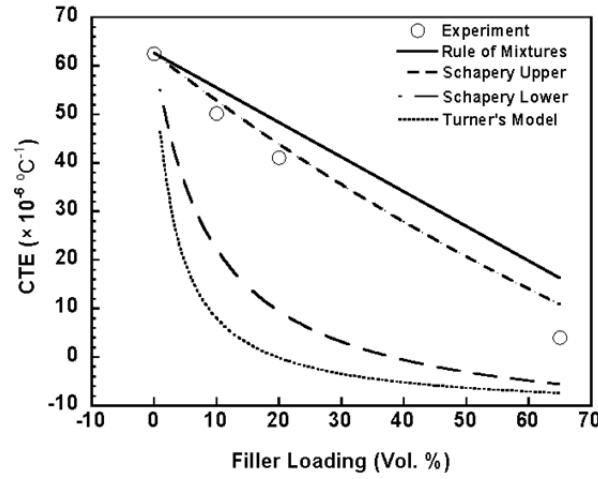
models that are used to predict CTE for polymer/filler composites are the rule of mixtures, Turners model, and Schapery's model.

Figure 3.9: Comparison of CTE values below T_g and corresponding values obtained from micromechanical models for various filler loadings.

The rule of mixtures involves computing the CTE of the composite based on the CTE of the filler (α_f), the CTE of the polymer matrix (α_m), and the filler volume fraction (ϕ_f), as shown in Equation 3.1 below:

$$\alpha_c = \alpha_f \phi_f + (1 - \alpha_f)(1 - \phi_f)$$

(3.1)

The rule of mixtures provides a good approximation of the composite CTEs, as shown in Figure 12; however, the values of CTE computed from Equation 3.1 are found to be higher than the values from experiments, especially at higher loadings since the possibility of interaction between the matrix and the filler is not accounted for [58-60]. Turner's model is inclusive of particle-matrix interactions by incorporating the bulk modulus of the filler (K_f) and the bulk modulus of the particle (K_m), as shown in Equation 3.2:

$$\alpha_c = \frac{(1 - \phi_f)K_m \alpha_m + \phi_f K_f \alpha_f}{(1 - \phi_f)K_m + \phi_f K_f}$$

(3.2)

The model assumes constant strain among all components of a sample and hence, the values of CTE from Turner's model are found to be much smaller than the values of CTE from experiments [58-60]. Schapery's model [61] derived on basis of free energy principles involves calculation of upper bound (α_c^u) and lower bound (α_c^l) values for CTE, as shown in Equations 3.3 and 3.4:

$$\alpha_c^l = \alpha_m + \frac{K_f}{K_c^u} \frac{(K_m - K_c^u)(\alpha_f - \alpha_m)}{(K_m - K_f)}$$

(3.3)

$$\alpha_c^u = \alpha_m + \frac{K_f}{K_c^l} \frac{(K_m - K_c^l)(\alpha_f - \alpha_m)}{(K_m - K_f)}$$

(3.4)

23

where K_c^u and K_c^l refer to the upper and lower bound values of the composite bulk modulus and can be determined as shown in Equations 3.5 and 3.6:

$$K_c^{\ l} = K_m + \cfrac{1}{\cfrac{1}{K_f - K_m} + \cfrac{3(1-\phi)}{(3K_m + 4G_m)}}$$

(3.5)

$$K_c^{\ u} = K_f + \cfrac{1}{\cfrac{1}{K_m - K_f} + \cfrac{3\phi}{(3K_f + 4G_f)}}$$

(3.6)

where G_m and G_f represent the shear modulus of the matrix and filler, respectively. The lower bound value, α_c^l is calculated by assuming constant strain in the Helmholtz free energy and is found to be much lower than the experimental values of CTE, similar to the results observed with Turner's iso strain model[58]. Conversely, α_c^u is calculated assuming constant stress in the Gibbs free energy and is found to be in reasonable agreement with the values of CTE from experiments. It is noted that upon comparing the above three models for predicting the CTE of ZrW_2O_8/phenolic resin composites, Tani and coworkers [26] also observed that the best description of the data was observed with Schapery's upper bound. Furthermore, the values from Schapery's upper limit was also found to provide a good description of the CTE behavior for BECy/silica nanocomposites in previous work [58].

The dynamic storage moduli (E') of the composites at 100 ^{o}C from DMA measurements are shown as a function of filler loading in Figure 3.10. The value of E' increases significantly with increasing filler content. For a filler loading of 10 vol. %, the E' value increases by 25 % compared to the corresponding value for neat BECy resin. For a filler loading of 65 vol. %, the E' value increases by 536 % compared to the neat resin. The large increase in E' is expected since some measurements [62] suggest the Young's modulus of ZrW_2O_8 to be around 88.3 GPa.
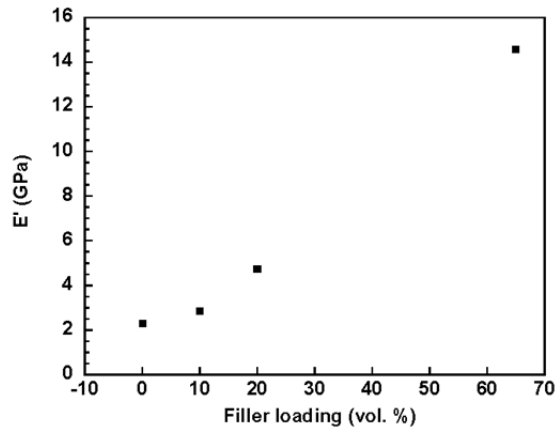
Figure 3.10: Comparison of E' from three point bending measurements in a DMA for various filler loadings at 100 ^{o}C.
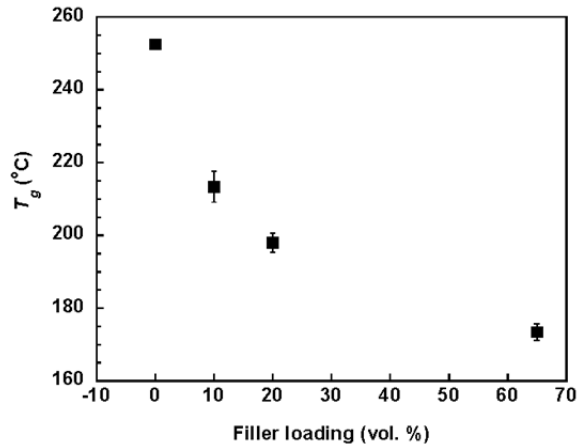

Figure 3.11: Dependence on glass transition of the composites on vol. % of ZrW_2O_8 filler loading.

The values of T_g determined from TMA measurements are plotted as a function of ZrW_2O_8 loading in Figure 3.11. The measurements clearly indicate that the incorporation of ZrW_2O_8 filler results in a systematic decrease in the T_g for the composites. The decrease in T_g

24

could be due to surface effects arising from the presence of OH groups in the ZrW_2O_8 particle surface, which have also been shown to catalyze the cure of BECy . It is noted that a decrease in T_g of BECy has also been reported upon incorporation of other fillers with OH groups at the surface such as nanosize alumina [63].

The effect of surface hydroxyl groups on the cure of BECy resin is further examined in this work through DSC cure studies. The dynamic DSC curing measurements for neat BECy resin and the $BECy/ZrW_2O_8$ composites are shown in Figure 3.12a-d. The value of ΔH for BECy is found to be 699.1 J/g (92.2 kJ/per cyanate equivalent), which is consistent with the values obtained in our previous work with BECy and also in the range reported in the literature for other cyanate ester resins (64,65). ΔH does not vary systematically with filler loading and has an average value of 691.2 J/g (91.2 kJ/per cyanate equivalent) for the ZrW_2O_8 reinforced resins The cure onset and peak temperatures obtained from the exotherms in Figure 6 are plotted as a function of heating rate in Figures 3.13 and 3.14, respectively. The exotherm onset and peak temperatures for BECy/ ZrW_2O_8 composites are found to be significantly lower than the corresponding values for neat BECy resin at every heating rate. Furthermore, the values of onset and peak temperatures exhibit a systematic decrease with increasing ZrW_2O_8 loading. The decrease in both onset and peak temperatures with ZrW_2O_8 loading is indicative of a significant increase in the cure rate. It is noted that the values of onset and peak temperatures for BECy/F-ZrW_2O_8 are also lower than the corresponding values for BECy, indicating an increase in cure rate upon incorporation of F-ZrW_2O_8.

Furthermore, the onset temperatures for the composite with 20 vol. % F-ZrW_2O_8 are found to be higher than the values for the composite with 20 vol. % as received ZrW_2O_8 with at any heating rate. Hence, the experiments demonstrate that at the same loading, silane treatment of ZrW_2O_8 results in delaying the onset of BECy cure in comparison with untreated ZrW_2O_8. However, although the peak temperatures for the composite with F-ZrW_2O_8 are found to be higher than the values for the composite with untreated ZrW_2O_8 at the slower heating rates of 7 and 5 K/min, no difference can be observed in the values at higher heating rates. The values of onset and peak temperatures for the neat BECy resin are found to be systematically lower than the values reported from the cure measurements in Chapter 2 due to the use of different batches of BECy for the two studies and also due to the tendency of BECy to crystallize during storage.
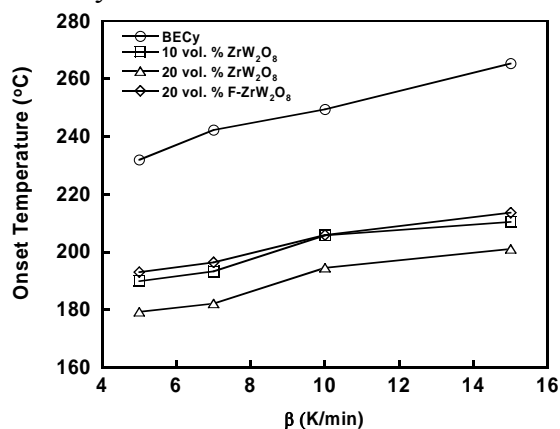
Figure 3.13: Comparison of onset temperature (T_o) for BECy resin and composites as a function of heating rate.
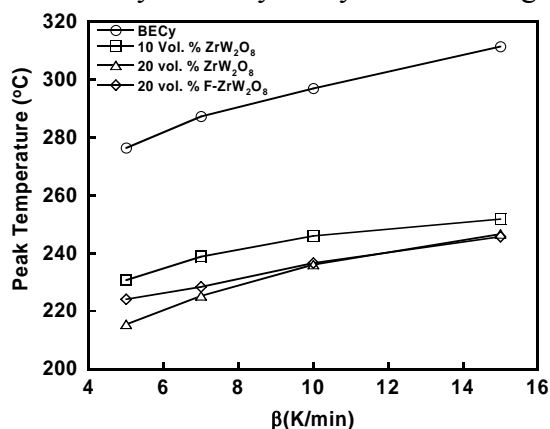
Figure 3.14: Comparison of peak temperature (T_p) for BECy resin and composites as afunction of heating rates.
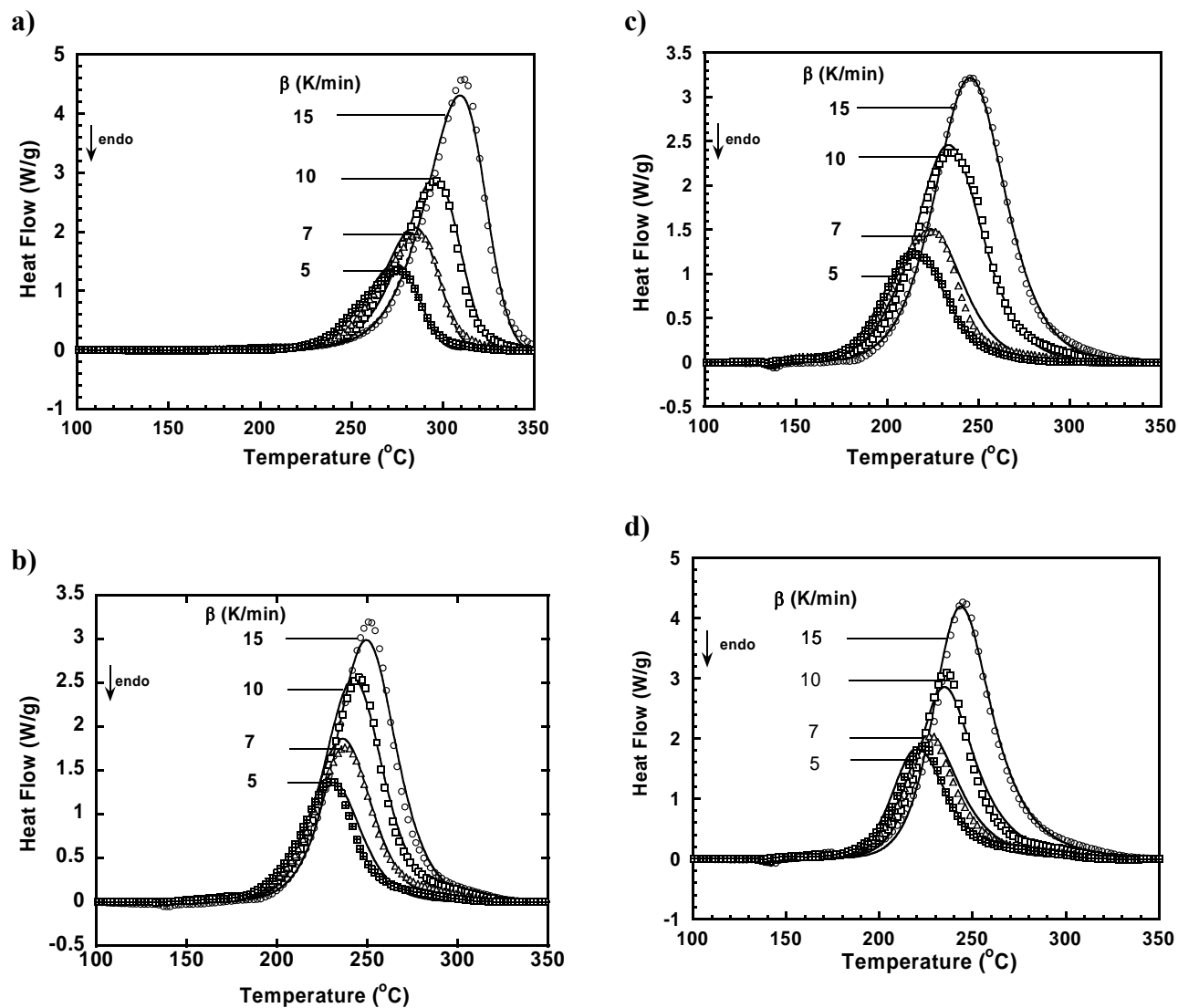
Figure 3.12 Dynamic DSC measurements at various heating rates for a) BECy b) BECy/10 vol. % ZrW_2O_8 c) BECy/20 vol. % ZrW_2O_8 d) BECy/20 vol. % F-ZrW_2O_8. The experimental data are represented by symbols and the solid lines are fits using an autocatalytic reaction model.

The increase in cure rate of BECy observed upon incorporation of ZrW_2O_8 is believed to be due to the presence and nature of hydroxyl groups on the filler particle surface. The catalytic effect of surface hydroxyl groups on BECy resin observed in this work is consistent with previous work in our laboratory, in which addition of silica [66] or alumina [63] that contain surface hydroxyl groups increased the curing rate of BECy. The surface hydroxyl groups can react with BECy and form a covalent bond between the particle and the polymer matrix leading to the observed increase in cure rate. The silane surface treatment involves a replacement of the OH groups with O-Si bonds and hence, the concentration of hydroxyl groups are reduced in the F-ZrW_2O_8 particles leading to a delay in the onset of cure when compared with BECy/ZrW_2O_8 composites.

The fits of the autocatalytic model $f(\alpha) = (1-\alpha)^n \alpha^m$ to the experimental curves are shown as the solid lines in Figure 3.12a-d. The model is found to provide an excellent fit to the experimental data and the kinetic parameters are tabulated in Table 3.1. The fact that the same autocatalytic model can describe the cure of BECy, the catalytic effect of the ZrW_2O_8 particles, and the delay in the cure as a consequence of silane surface treatment indicates that the overall reaction mechanism is not significantly altered upon incorporation of the filler particles.

Table 3.1: Kinetic parameters obtained from n^{th}-order autocatalytic model fit.

Sample	Log (A/s^{-1})	E_a (kJ/mol)	n	m
BECy	4.89	74.2	0.87	0.58
10 vol.% ZrW_2O_8	10.27	119.8	1.51	0.32
20 vol.% ZrW_2O_8	5.04	67.3	1.36	0.55
20 vol.% F-ZrW_2O_8	7.78	92.6	1.8	0.58

The delay in cure behavior of BECy upon incorporation of F-ZrW_2O_8 is likely a result of partial steric shielding of the catalyzing hydroxyl groups on the ZrW_2O_8 by the silane groups in GPS and is consistent with the higher onset temperatures shown in Figure 3.13 for these systems. These differences in cure behavior of BECy as a consequence of filler loading and type need to be accounted for to optimize the thermomechanical properties of the composites.

DSC measurements of the composite T_g can also be used to examine the impact of filler loading and the silane surface treatments. As shown in Figure 3.15, the T_g of BECy decreases by up to 13.5 ^{o}C and 14.5 ^{o}C upon incorporation of 10 and 20 vol. % ZrW_2O_8 particles, respectively; however, the T_g reduction is substantially mitigated upon performing the silane treatment of the ZrW_2O_8. Upon incorporation of 10 vol. % F-ZrW_2O_8, the T_g of composite increases by 3.9 ^{o}C compared to BECy. Upon incorporation of 20 vol. % F-ZrW_2O_8, the T_g is found to be reduced by 6 ^{o}C compared to BECy, which is a significant improvement compared to untreated particles at the same loading. The enhancement in T_g could be due to the improved compatibility of F-ZrW_2O_8 with the BECy polymer matrix as a consequence of the silane surface treatment.
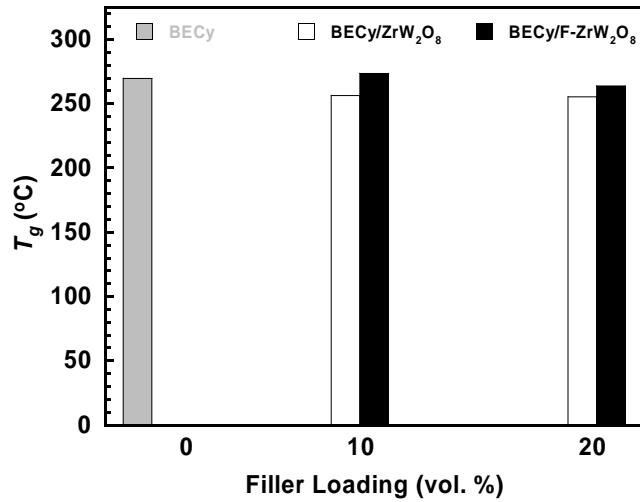
Figure 3.15: Effect of ZrW_2O_8 and F-ZrW_2O_8 loading on T_g.

3.4   Conclusions

In this work, BECy/ZrW_2O_8 composites with three different filler loadings of 10, 20, and 65 vol. % were prepared. The BECy/ZrW_2O_8 composites exhibit a γ-α phase transition followed by a α-β phase transition in the heating measurements, although the α-β transition is not observed in heat flow measurements in the DSC. The CTE of the composites is found to decrease with increasing ZrW_2O_8 filler loading. The maximum decrease in CTE is observed for the 65 vol. % filler loading with CTE decreasing by 92 % below T_g and 88 % above T_g, in comparison with the neat resin. The CTE measurements are best described by the values calculated from Schapery's upper bound. The T_g of the composite is found to decrease with increasing filler loading, possibly due to the presence of hydroxyl groups on the particle surface although the dynamic storage modulus increases significantly. However, the reduction in T_g observed upon filler loading in BECy/ZrW_2O_8 composites was substantially mitigated when the ZrW_2O_8 particles were functionalized with a silane surface treatment. Although the silane treated ZrW_2O_8 particles were also found to catalyze the cure of BECy, the dynamic DSC experiments indicate that the onset of the cure is delayed in comparison with BECy/ZrW_2O_8 composites of the same loading. Hence silane functionalization is identified as a potential strategy for mitigation of the extent of reduction of glass transition upon incorporation of inorganic nanoparticles in the BECy matrix.

CHAPTER 4: Synthesis, Processing, and Characterization of ZrW$_2$O$_8$ Nanoparticles with Different Morphologies

4.1   Introduction

As described in Chapter 1, the synthesis of ZrW$_2$O$_8$ nanoparticles has been accomplished through either sol-gel [22,27] or hydrothermal methods [29,30]. However, detailed characterization of the thermal expansion behavior in these unique zirconium tungstate nanoparticles has never been reported in the literature. Recent studies [67-69] have shown that the CTE of some materials may be dramatically different at the nanoscale in comparison to the bulk. For example, nanosize copper oxide (CuO) exhibits a large negative CTE (-3.7×10^{-5}), even greater than zirconium tungstate at cryogenic temperatures, whereas bulk CuO exhibits a large positive CTE in the same temperature range [67]. Although, the CTE of bulk ZrW$_2$O$_8$ has been reported over a wide range of temperatures and pressures in previous work [19,70,71], the CTE behavior in ZrW$_2$O$_8$ nanoparticles has not been reported in the literature. Considering the increasing interest in utilizing the negative CTE nanoparticles for a variety of nanocomposites with tailored thermal expansion, characterization of the negative CTE behavior of these nanoparticle sand a comparison with the behavior observed for bulk zirconium tungstate is crucial.

This chapter describes the characterization of CTE for ZrW$_2$O$_8$ nanoparticles with different morphologies from sol-gel and hydrothermal methods using isothermal XRD measurements over a broad temperature range. The CTE values of the nanoparticles are also compared the CTE of bulk ZrW$_2$O$_8$. As noted earlier in Chapter 1, synthesis of zirconium tungstate nanoparticles by sol-gel techniques has been reported to result in complete particle agglomeration upon employing traditional drying methods following synthesis. Hence, in this work, the potential for produce non agglomerated nanoparticles by using a freeze drying method to dry the particles following synthesis was also examined.

4.2   Methodology

4.2.1 Materials

Zirconium dichloride oxide octahydrate (ZrOCl$_2$.xH$_2$O, Assay. 99.5%) was purchased from Alfa Aesar (Ward Hill, MA) and stored in a glove box under nitrogen. Sodium tungstate dihydrate (Na$_2$WO$_4$. 2 H$_2$O, ACS, 99.5-101.0%) was purchased from Sigma Aldrich (St Louis, MO). Ammonium meta tungstate hydrate (NH$_4$)$_6$H$_2$W$_{12}$O$_{40}$. xH$_2$O,(99.9%) was purchased from Strem Chemicals (Newburyport, MA). The surfactant Tergitol NP 9 was purchased from Sigma Aldrich. Bulk ZrW$_2$O$_8$ was purchased from Alfa Aesar with an average particle size of 75 μm was used after heating above 200 $^{\circ}$C to ensure the absence of γ-phase.

4.2.2 Synthesis of ZrW$_2$O$_8$ nanoparticles

Sol-gel /Reverse Micelle route- This method was based on the previous work in the literature [22,27] with some modifications to minimize particle agglomeration. Zirconium dichloride oxide octa hydrate (7.5 mmol) was added to 3 mL of deionized water and ammonium meta tungstate hydrate (1.25 mmol) was added to 6 mL of deionized water. The two reactants were mixed dropwise in a vial to prepare a clear solution. The reactant mixture was added

dropwise to a 500 ml round bottom flask containing cyclohexane as the oil phase, Tergitol NP 9 as the surfactant, and hexanol as the cosurfactant. The mixture was stirred continuously for 4 hours after which, ethanol (130 mL) was added immediately resulting in a white precipitate. The solution was further stirred for 1 hour and the white precipitate was separated out by centrifuging. The precipitate was washed repeatedly with ethanol followed by deionized water. The precipitate was mixed with 125 mL of deionized water and transferred to a 500 mL round bottom flask. Subsequently, 125 mL of 6M hydrochloric acid was slowly added to the flask and the mixture was allowed to reflux for 2 days under stirring. The precipitate was separated out by centrifuging and washed repeatedly with deionized water. To eliminate agglomeration of the particles during drying, we added a unique step to the procedure where the solution containing the particles was freeze dried using a Virtis Ultra 35 model freeze dryer (Gardnier, NY) at 24 ^{o}C for one day. The freeze dried powder was calcined at 600 ^{o}C for 6 hours to yield a yellowish white powder.

Hydrothermal route- The ZrW_2O_8 nanoparticles were synthesized by scaling up the hydrothermal method reported by Sharma and coworkers [72]. First, 1.28 g of $ZrOCl_2 \cdot xH_2O$ and 1.65 g of $Na_2WO_4 \cdot 2 H_2O$ were dissolved separately in 8 mL deionzed water and mixed dropwise in a 125 mL Teflon-lined Parr bomb. Next, 15 g of NaCl and 21.6 mL of 70 % perchloric acid was added to 13 mL of deionized water and heated to dissolve the salt. The mixture was allowed to react at 130 ^{o}C for 24 hours. The precipitate was washed and subsequently dried under vacuum at 70 ^{o}C. The powder was calcined at 600 ^{o}C for 30 minutes to yield a white powder. It is noted that subsequent work by Kozy and coworkers [73] have shown that smaller and more dispersed nanoparticles can be synthesized from the hydrothermal method through incorporation of alcohols such as butanol within the reaction mixture. However, inclusion of alcohols has also been shown to greatly expedite the rate of an "autohydration" phenomenon for the hydrothermal nanoparticles, which leads to water absorption at room temperature [74] and hence, was not employed in this work.

4.2.3 Particle characterization

Scanning electron microscopy (SEM) of the nanoparticles was performed using a JEOL JSM 840A scanning electron microscope. Transmission electron microscopy (TEM) was performed was performed using a JEOL 2100 200 kV microscope. The particle size distribution of the nanoparticles was examined using a Shimadzu SA-CP3 centrifugal particle size analyzer. The moisture absorption of the nanoparticles was studied using a Q50 thermogravimetric analyzer (TGA) from TA Instruments upon heating at 20 ^{o}C/min under air purge. The structural features of the nanoparticles were compared using a Renishaw InVia Raman spectrometer. The XRD spectra at ambient temperatures were obtained using a Scintag powder XRD instrument. Isothermal XRD measurements at various temperatures were performed in a PAnalytical instrument equipped with a temperature controlled hot stage. The diffraction data was collected at constant temperatures at the intervals of 25 ^{o}C and 50 ^{o}C between 25-250 ^{o}C and 250 to 600 ^{o}C, respectively. The temperature of the hot stage was raised at a rate of 5 ^{o}C /min in between each measurement temperature. Data was collected in steps of 0.02^o from 10° to 90° for an exposure time of 100 s at each temperature. Silica was used as an internal calibration standard. The increase in height of sample stage arising from expansion of the alumina support rod was compensated using a stepper motor.

4.3   Results and discussion

A representative scanning electron microscopy (SEM) image of the ZrW_2O_8 nanoparticles synthesized by the sol-gel/reverse micelle approach are shown in Figure 4.1a. The morphology consists mainly of parallelepiped shaped nanoparticles, although some larger plate-like particles are also observed. The freeze drying procedure employed in this work is successful in preventing the agglomeration of the parallelepipeds in contrast to loss of nanostructures reported by Schnabel and coworkers [27]. The parallelepipeds are typically 1- 2 μm long and 100-200 nm thick as shown in Figure 4.1b. The median particle size determined using a particle size analyzer was found to be 0.36 μm.
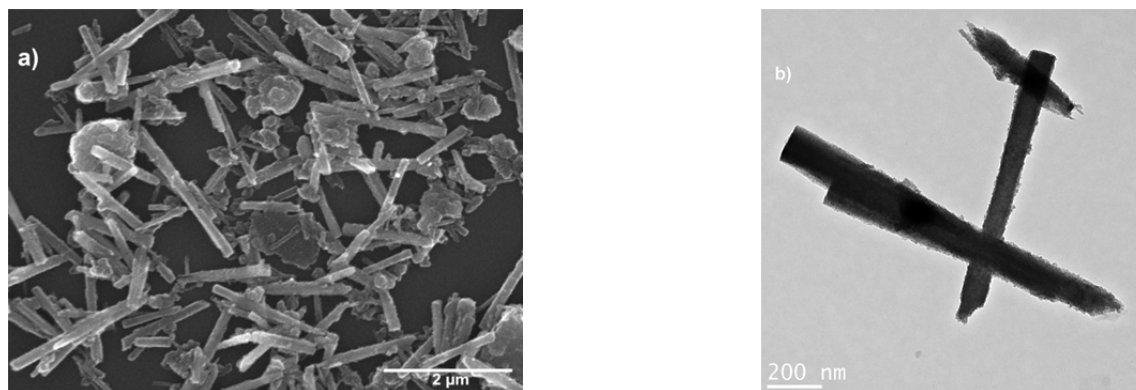
Figure 4.1: Morphology ofZrW$_2$O$_8$ nanoparticles synthesized by sol-gel method a) SEM image b) TEM image
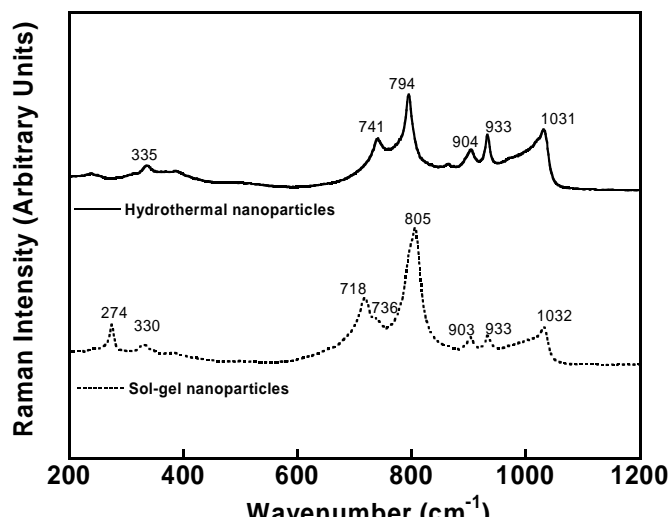
The SEM image of the ZrW_2O_8 nanoparticles synthesized from the hydrothermal method is shown in Figure 4.2a. Unlike the particles synthesized by the sol-gel method, the particles are characterized by a distribution of bundles with "whisker-like" morphology, which are more clearly illustrated in Figure 4.2b. Particle size measurements indicate that the particles from the hydrothermal approach are characterized by a median size of 0.19 μm.
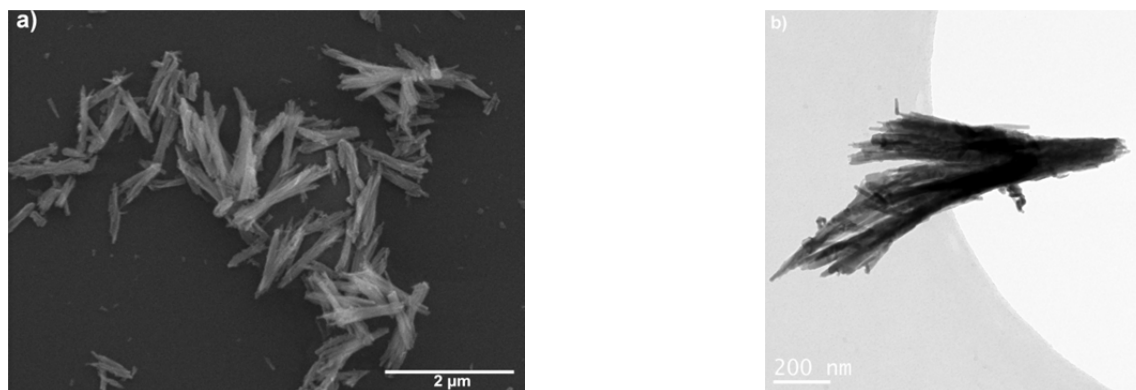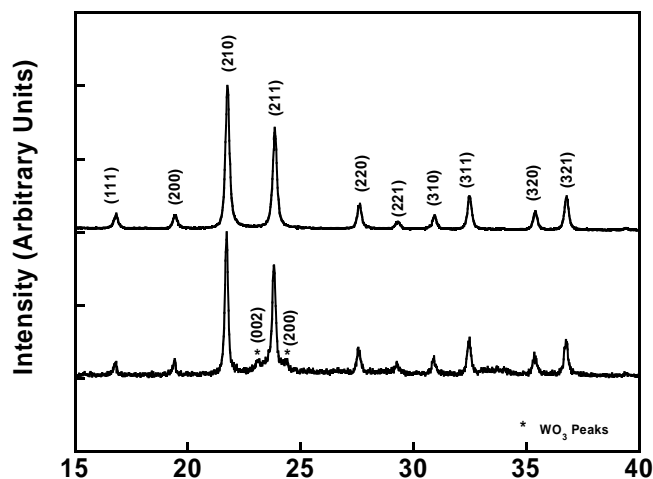

Figure 4.2: Morphology of ZrW_2O_8 nanoparticles synthesized by hydrothermal method a) SEM image b) TEM image

The room temperature Raman spectra for the hydrothermal and the sol-gel nanoparticles are compared in Figure 4.3. The Raman peaks at 1031 and 933 cm^{-1} arise from symmetric stretching vibrations of the oxygen atom around the tungsten atom in the WO$_4$ tetrahedra, while the peaks between 904 to 741 cm^{-1} can be attributed to asymmetric stretching vibrations [75,76]. Previous studies have reported that the γ phase, which also exists at room temperature can be distinguished from α phase zirconium tungstate by the absence of the peaks at 904 and 932 cm^{-1} and by the occurrence of significant peak splitting at 794 cm^{-1} [75,76]. The spectra shown in Figure 4.3 clearly illustrate that the nanoparticles synthesized by both methods in this work

Figure 4.3: Comparison of Raman spectra for ZrW$_2$O$_8$ nanoparticles synthesized by sol-gel and hydrothermal methods.

primarily comprise of α phase zirconium tungstate. However, the nanoparticles synthesized from the sol-gel method exhibit some differences in the Raman spectra such as the presence of peaks at 274 and 718 cm^{-1} and a shift in asymmetric stretching peak from 794 to 806 cm^{-1}. These differences can be attributed to the presence of a small amount of tungsten oxide in the sol-gel synthesized nanoparticles. The presence of tungsten oxide as a byproduct upon synthesis of ZrW$_2$O$_8$ through sol-gel methods has been reported previously in the literature [27,77].

The room temperature XRD spectra for the nanoparticles synthesized from the sol-gel method are shown in Figure 4.4. Although, the peaks are representative of cubic zirconium tungstate, the additional peaks at 23.1° and 24.3° reveal the presence of tungsten oxide, in agreement with the Raman results. Quantitative analysis of the XRD spectra reveals the presence of almost 10 wt. % WO$_3$. Schnabel and cowokers [27] also reported the presence of 13 wt. % tungsten oxide in ZrW$_2$O$_8$ nanoparticles synthesized following the sol-gel/reverse micelle approach of Sullivan and Lukehart [22]. In this work, attempts to minimize the extent of WO$_3$ through optimization of calcination time and atmosphere did not result in significant improvements. On the


Figure 4.4: Comparison of XRD spectra for ZrW$_2$O$_8$ nanoparticles synthesized by sol-gel and hydrothermal methods.

other hand, the XRD spectra of the ZrW_2O_8 nanoparticles obtained from the hydrothermal approach indicates that that the product is crystalline ZrW_2O_8, with no byproducts such as WO_3, as shown in Figure 4.4.

The lattice parameters obtained from isothermal XRD measurements at various temperatures for the sol-gel and hydrothermal nanoparticles are compared in Figure 4.5. In the case of nanoparticles synthesized by the sol gel route, the presence of WO_3 phase was also taken into consideration by fitting both ZrW_2O_8 and WO_3 phases simultaneously. Moreover, there was no significant overlap in the WO_3 and ZrW_2O_8 peaks in XRD data. Therefore, no interference in estimated lattice parameters of ZrW_2O_8 was expected due to the presence of about 10% WO_3. The lattice parameters for the nanoparticles decrease with increasing temperature in both cases, which confirms the negative CTE behavior in ZrW_2O_8 nanoparticles. Furthermore, in both the cases, a change in slope can be observed around 150 °C, signaling a transition from the α phase to the β phase.
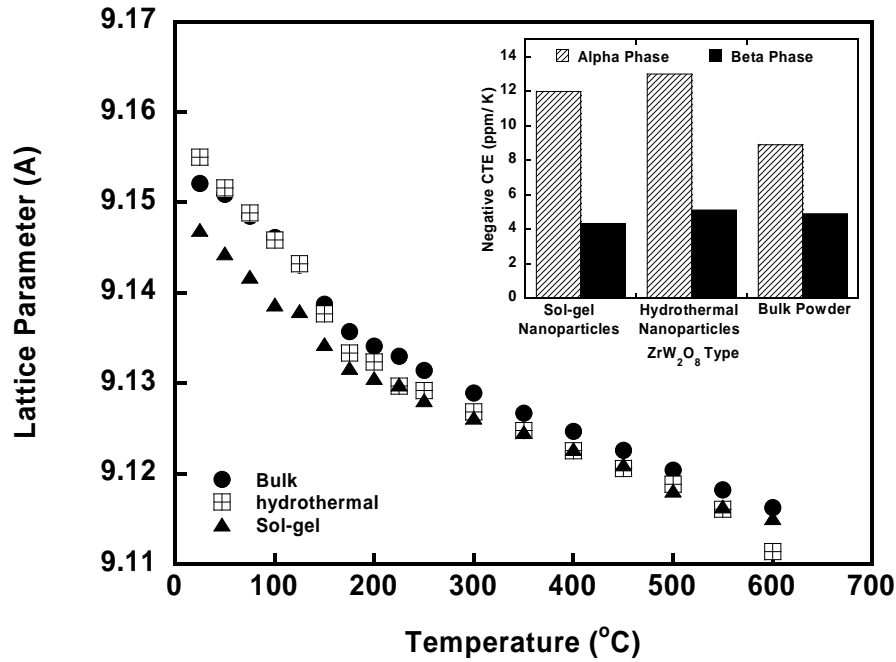
Figure 4.5: Lattice constants obtained for the nanoscale and bulk ZrW_2O_8 as a function of temperature. A comparison of negative CTE values for the nanoparticles and bulk ZrW_2O_8 is shown in the inset.

The temperature range of transition is also similar to the temperature range reported in previous work [71] for α to β phase transition in micron size ZrW_2O_8 particles. The lattice parameters from the XRD measurements can be used to determine the CTE (α) for each phase according to:

$$\alpha = \frac{1}{a_0} \frac{da}{dT}$$

(1)

where, a_0 is the initial lattice parameter and da/dT is the change in lattice parameter with temperature. The lattice parameter data obtained in the temperature range of 25 °C to 100 °C was used for determination of α phase CTE while the data from 200 °C to 600 °C was used to estimate the CTE of the β phase. For the bulk ZrW_2O_8 powder, the α phase CTE is -8.9 × 10^{-6} K⁻

[1] and the β phase CTE is -4.9×10^{-6} K^{-1}, in excellent agreement with previously reported values in the literature [19,71]. For the sol-gel nanoparticles , the α phase and β phase CTE values are -12.0×10^{-6} K^{-1} and -4.3×10^{-6} K^{-1},while the hydrothermal nanoparticles are characterized by α phase and β phase CTE values of -13.0×10^{-6} K^{-1} and -5.1×10^{-6} K^{-1}.   The values of negative CTE for the hydrothermal and sol-gel nanoparticles do not differ significantly indicating a lack of dependence of the negative CTE behavior on the particle morphology. Interestingly, although nanosize and bulk ZrW_2O_8 exhibit similar values of CTE in the high temperature β phase, the nanoparticles exhibit an even more negative in the α phase in comparison to bulk zirconium tungstate, as demonstrated in the inset of Figure 4.5.

The differences in the α phase CTE between nanosize and bulk ZrW_2O_8 warrants further examination. A possible reason for the significant differences in the thermal contraction only in the temperature range corresponding to the α phase maybe the differences in extent of adsorbed moisture carried by the particles. It is well established that adsorption of moisture can lead to expansion of porous materials as a consequence of decrease in surface forces. Similarly, desorption of adsorbed moisture leads to contraction of for porous materials such as ceramic oxides [78].   A comparison weight loss curves for bulk and nanosize ZrW_2O_8 particles, measured by TGA on heating at 20 K/min, is shown in Figure 4.6.   The TGA curves demonstrate that the weight loss corresponding to the loss of adsorbed moisture is found to be highest for the hydrothermal nanoparticles and the lowest for bulk zirconium tungstate. The greater amount of adsorbed moisture for the nanoparticles can be explained by their greater surface area in comparison to bulk ZrW_2O_8. The negative CTE of hydrothermally synthesized ZrW_2O_8 is higher

Figure 4.6: Comparison of weight loss due to adsorbed moisture measured by TGA for ZrW_2O_8 nanoparticles and bulk ZrW_2O_8.

than the negative CTE of both bulk ZrW_2O_8 and sol-gel ZrW_2O_8 in the temperature range corresponding to the α phase due to the additional shrinkage as a consequence of progressively greater desorption of the adsorbed moisture taking place with increasing temperature before 125 °C. However, once all the water was desorbed no significant difference in CTE could be observed in the temperature range corresponding to the β phase. Similarly, the sol-gel nanoparticles also contain greater extents of adsorbed moisture in comparison to bulk ZrW_2O_8, which results in more shrinkage when compared to bulk ZrW_2O_8, due to moisture desorption on heating.

It is noted the effect of adsorbed moisture observed in this work should be differentiated from the effect of water molecules incorporated in to the crystal framework of ZrW_2O_8. Duan and coworkers have shown that ZrW_2O_8 actually exhibits dramatic lattice contraction upon incorporation of water molecules in to the lattice framework due to a decrease in bond distances. However, insertion of water in to the crystal framework was possible only by hydrating the material at elevated temperatures such as 180 °C in a high pressure reaction. The process was found to be reversible by heating the material to 200 °C, which resulted in removal of water from the framework and expansion of the lattice, which is the opposite trend to that reported in this

work. However, such a result is not unexpected since the nanoparticles synthesized in the work were not subjected to harsh hydration conditions. Hence, the moisture present on the surface of the particles is simply adsorbed moisture, which during desorption from the surface contributes to additional lattice shrinkage, as expected for porous ceramic materials.

The results in this work confirm that ZrW_2O_8 nanoparticles do exhibit a strong negative CTE behavior over a wide temperature range, which is of significant interest for their use as negative CTE component of variety of nanocomposites. While no major differences can be observed in the negative behavior between nanosize and bulk ZrW_2O_8 in the high temperature β phase, the differences in the α phase can be explained by systematic differences in extent of adsorbed moisture.

4.4 Conclusions

In conclusion, the CTE of nanosize ZrW_2O_8 was characterized for the first time in this work for nanoparticles synthesized through sol-gel and hydrothermal methods. The ZrW_2O_8 obtained from the sol-gel technique comprised a heterogeneous distribution of nanosize parallelepipeds along with larger plate like particles. The freeze drying procedure employed in this work was successful in preventing agglomerating of nanostructures in the sol-gel approach. The nanoparticles obtained from the hydrothermal method were characterized by a whisker-like morphology. Raman measurements demonstrated that the nanoparticles synthesized through both methods were in the α phase, although some changes in the spectra was observed for sol-gel synthesized nanoparticles due to the presence of tungsten oxide. Isothermal XRD measurements revealed that the nanoparticles exhibit a contraction in lattice parameter and a large negative CTE behavior. The values of CTE of the nanoparticles obtained from the two methods were found to be similar in either α or the β phase, and hence, not influenced by particle morphology. However, the α phase CTE of the nanoparticles was found to be more negative in comparison to bulk ZrW_2O_8 and was demonstrated to be due to additional shrinkage arising from water desorption, while the values of CTE for the β phase were similar.

CHAPTER 5: BECy/ZrW$_2$O$_8$ Nanocomposites with Tailored Thermal Expansivity

5.1   Introduction

Negative CTE fillers offer tremendous potential for CTE reduction of the polymer matrix and can lead to polymer composites with tailored thermal expansivities. Among the few materials that exhibit negative thermal expansion behavior, zirconium tungstate exhibits one of the largest isotropic negative CTE values reported [19]. More recently, Zheng and coworkers [77] reported that nanosize copper oxide particles exhibit a negative CTE that is an order of magnitude greater than ZrW$_2$O$_8$ due to magnetic interactions between neighboring atoms. However, unlike copper oxide nanoparticles which exhibit negative CTE behavior only at cryogenic temperatures, ZrW$_2$O$_8$ exhibits negative CTE behavior over a broad temperature range from -263 ^{o}C to 777 ^{o}C [19], which makes it an attractive filler for polymer composites.

The effect of incorporating micron size ZrW$_2$O$_8$ particles in BECy was described in detail in Chapter 3. We observed that the CTE of BECy could be reduced by up to 92 % upon incorporation of 65 vol. % micron size ZrW$_2$O$_8$. However, the incorporation of such high filler loadings leads to significant processing constraints, not conducive to the preparation of PMCs. A reduction in the scale of the reinforcement from micron size to nano scale may facilitate better filler dispersion and a reduction in the magnitude of thermally induced displacements. However, the potential for development of polymer nanocomposites through incorporation of zirconium tungstate nanoparticles in a polymer matrix has not received extensive attention, with only one prior study [22] being reported in the literature. Sullivan and coworkers[22] developed ZrW$_2$O$_8$/polyimide thin film nanocomposites with low values of CTE; in their work, ZrW$_2$O$_8$ nanoparticles were synthesized through a combination of sol-gel processing and reverse micelle methods. However, as described in Chapter 4, such the sol-gel based methods for synthesis of ZrW$_2$O$_8$ result in heterogeneous distribution of particle size along with small amounts of tungsten oxide impurity. Hydrothermal methods which involve acid digestion of precursors at high temperatures and pressures were found to result in highly crystalline, pure ZrW$_2$O$_8$ nanoparticles, which are suitable for preparation of polymer nanocomposites.

This chapter describes the development of thermosetting polymer nanocomposites obtained through incorporation of hydrothermally synthesized ZrW$_2$O$_8$ nanoparticles in BECy resin. A reduction in CTE of the BECy matrix would reduce the extent of mismatch in CTE with fiber reinforcements, mitigate residual stresses following the cure and improve dimensional stability. In this work, up to 10 vol. % of ZrW$_2$O$_8$ nanoparticles synthesized through hydrothermal methods is incorporated in BECy resin in order to examine potential for CTE reduction. This is the first study to develop bulk polymer nanocomposites with negative CTE ZrW$_2$O$_8$ nanoparticles. This work seeks to develop a detailed understanding of the effect of the negative CTE nanoparticles on the processing and thermal characteristics of BECy, which is crucial for development of dimensionally stable hybrid polymer composites with these materials. In Chapter 3, a silane surface treatment was demonstrated to be effective in preventing a decrease in the glass transition temperature (T_g) of BECy upon incorporation of micron size ZrW$_2$O$_8$ particles, even at a loading of 10 vol. %. Hence, the effect of silane treated negative CTE nanoparticles loading functionalization on the CTE and thermal properties of the BECy matrix is examined in this chapter.

5.2   Methodology

5.2.1   Materials

Zirconium dichloride oxide octahydrate was purchased from Alfa Aesar (Ward Hill, MA) and stored in a glove box under nitrogen. Sodium tungstate dihydrate was purchased from Sigma Aldrich (St Louis, MO). The BECy resin used was EX 1510 resin obtained from Tencate Technologies (Morgan Hill, CA). The catalyst (EX 1510 B) required for curing the resin was also obtained from Tencate Technologies and added at a ratio of 3 parts catalyst per hundred parts resin.

5.2.2   Synthesis and Surface Treatment of ZrW_2O_8 nanoparticles

The ZrW_2O_8 nanoparticles were synthesized by the hydrothermal method described in Chapter 4. The ZrW_2O_8 nanoparticles were functionalized using glycidyloxypropyl trimethoxysilane (GPS). In a 250 ml round bottom flask, 6.5 g of ZrW_2O_8 nanoparticles and 7.3 ml of GPS were dispersed in 125 ml of dry THF and the mixture was allowed to reflux for 2 days at 95 ^{o}C in a nitrogen atmosphere, under constant stirring. The particles were separated by centrifuging and rinsed repeatedly with THF to remove the excess silanes. Subsequently, the ZrW_2O_8 particles were dried at room temperature for 2 days and then dried at 100 ^{o}C under vacuum.

5.2.3 Preparation of BECy/ZrW_2O_8 nanocomposites

BECy/ZrW_2O_8 nanocomposites with various filler loadings were prepared by mixing the required amount of dried ZrW_2O_8 particles in BECy resin. The particles were dispersed in the resin by mixing for 3 hours in an ultrasonic water bath. The mixture was transferred to a vacuum oven and degassed for 1 hour at room temperature. The composites were cured up to the gel point at 160 ^{o}C in a rotating oven to maintain filler dispersion during the cure. The composite was subsequently transferred to a convection oven where it was further cured at 180 ^{o}C for 2 hours followed by a post cure at 250 ^{o}C for 2 hours.

5.2.4   Characterization of ZrW_2O_8 nanoparticles

The effect of the silane surface treatment of ZrW_2O_8 particles was examined by heating a small quantity of the treated and untreated powders at 20 K/min to 800 ^{o}C under air in a Q50 TGA from TA instruments (New Castle, DE).   The functionalization of the nanoparticle surface with the silane was verified by using a Hyperion Fourier Transform Infrared (FTIR) spectrometer from Bruker Optics (Billerica, MA).

5.2.5   Characterization of BECy/ZrW_2O_8 nanocomposites

The effect of nanoparticle loading on the viscosity of BECy resin was examined by steady state rheology measurements in an AR 2000ex stress controlled rheometer from TA Instruments. Approximately 0.25 ml of the suspension was injected between parallel plates and the shear rate was increased from 0.1 to 100 s^{-1}, to examine the effect of filler loading and shear rate on suspension viscosity. Differential scanning calorimetry (DSC) was used to examine the effect of the nanoparticle loading on the resin cure behavior. The DSC measurements were performed by adding approximately 10 mg of the resin without catalyst in a hermetically sealed aluminum pan. The measurements were performed on heating at 10 ^{o}C/min in a Q20 DSC from TA Instruments. Transmission electron microscopy (TEM) of the fully cured nanocomposites

was performed using a JEOL 2100 200 kV microscope. The samples were prepared for imaging by ultramicrotomy. The filler loading in the nanocomposites was also verified using TGA measurements by heating three samples for each nanocomposite system to 850 °C at 20 °C/ min under air. Thermomechanical analysis (TMA) measurements were performed for five samples at each loading with a Q400 thermomechanical analyzer from TA Instruments to determine the CTE of the polymer nanocomposites. The samples with dimensions of $3 \times 3 \times 3$ mm were first heated at 5 °C/min to 300 °C to erase previous thermal history. Following cooling at 5 °C/min, a second heating scan at 5 °C/min was performed to determine the CTE of the composites. DMA measurements were performed for four samples at each loading using a Q800 dynamic mechanical analyzer from TA Instruments in tension mode with amplitude of 5 μm and frequency of 1 Hz. Samples with dimensions of $15 \times 3 \times 1.5$ mm were heated up to 300 °C at 5 °C/min.

5.3   Results and Discussion

The silane functionalization of the ZrW_2O_8 nanoparticles was verified by TGA measurements, as shown in Figure 5.1. ZrW_2O_8 exhibits a weight loss of 2.76 % over the measurement range, which can be attributed to the loss of physically adsorbed water (100-150 °C) and the loss of surface hydroxyl groups. The overall weight loss of the silane treated ZrW_2O_8 particles is found to be greater due to the decomposition of the organic constituents of GPS. The FTIR spectra of the untreated and silane treated nanoparticles are compared in Figure 5.2. The silane treated particles exhibit some additional peaks at 2865 cm^{-1} and 2938 cm^{-1} due to C-H stretching and at 1099 cm^{-1} due to Si-O stretching. The presence of the additional peaks for the treated nanoparticles confirms the functionalization of hydroxyl groups on nanoparticle surfaces with GPS.
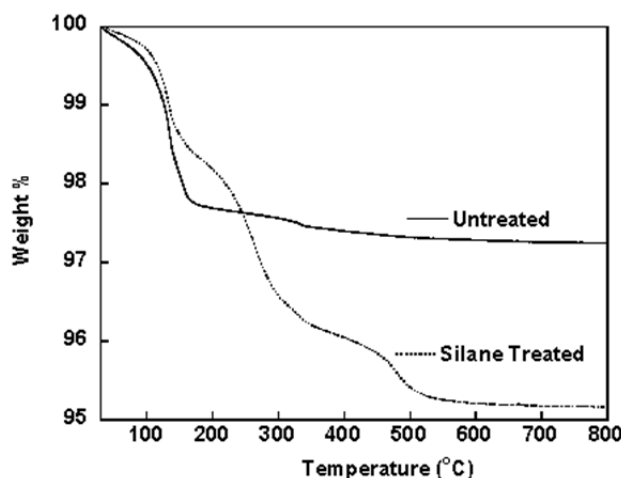
Figure 5.1: Comparison of TGA heating scans for untreated and silane treated ZrW_2O_8 nanoparticles.
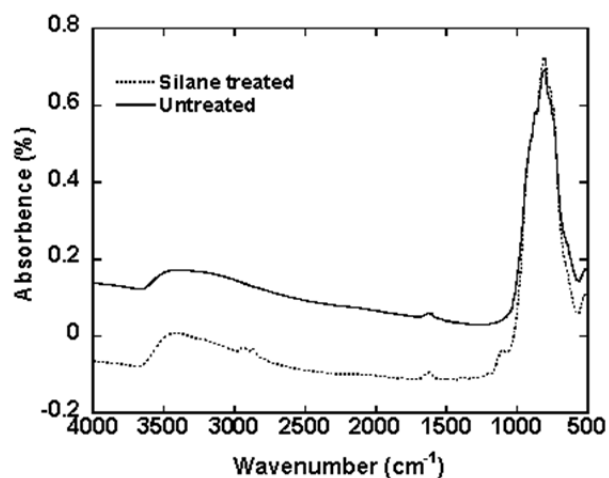
Figure 5.2: Comparison of FTIR spectra for untreated and silane treated ZrW_2O_8 nanoparticles.

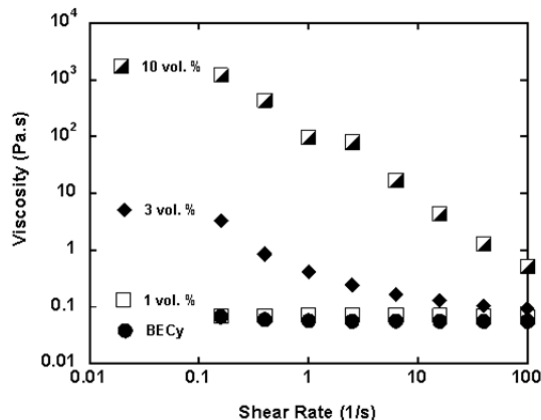Steady state rheology measurements were used to examine the effect of the GPS treated ZrW_2O_8 particles on the viscosity of BECy resin at room temperature (23 °C), as shown in Figure 5.3. The viscosity increases systematically with filler loading, as expected. The viscosity
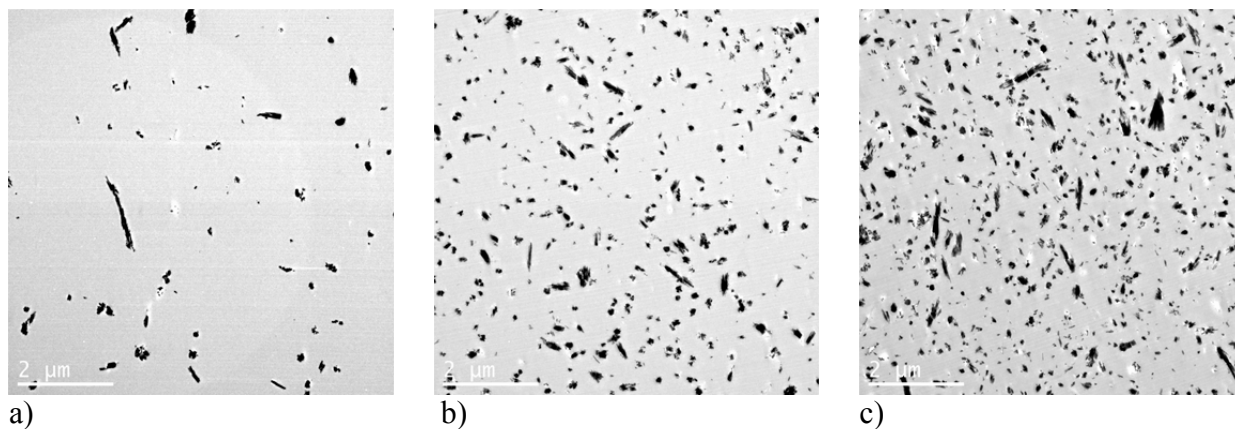
increases by almost four orders of magnitude upon incorporation of 10 vol. % nanoparticles. However, the low viscosity of BECy resin (<0.1 Pa.s) ensured that the nanocomposite could still be processed. While BECy exhibits near Newtonian behavior with increasing shear rate, the BECy/ZrW_2O_8 nanocomposites exhibit shear thinning behavior with the viscosity decreasing with increasing shear rate. The shear thinning behavior of BECy has been observed in earlier work [66] upon incorporation of silica nanoparticles, which also contain surface hydroxyl groups. The dramatic shear thinning effect also suggests that shear mixing could be an effective technique for incorporation of these

Figure 5.3: Steady state rheology measurements that demonstrate the effect of nanoparticle loading on the resin viscosity as a function of the

nanocomposites with higher filler loadings during preparation of fiber reinforced composites.

The TEM images of the fully cured nanocomposites with various filler loadings are shown in Figures 5.4 a-c. The images reveal attainment of high levels of dispersion for all loadings examined in this work. Furthermore, the images also indicate that the whisker bundles are broken up in to smaller fragments as a consequence of the ultrasonic processing techniques employed in this work.


a)   b)   c)

Figure 5.4: TEM images of BECy/ZrW_2O_8 nanocomposites at various loadings a)1 vol. % b) 3 vol. % c) 10 vol. %

The filler content in the nanocomposites was examined through TGA measurements, as shown in Figure 5.5. While BECy completely degrades upon heating to 850 $^{\circ}$C under air, the ZrW_2O_8 nanoparticles incur only a small weight loss, which can be used to verify the filler loading. The final weight loss from the TGA measurements in Figure 5.5 increases with increasing nanoparticle loading, as expected. An estimate of the extent of filler dispersion can also be made by determining the residual weight from different sections of the cured nanocomposites, as shown in the inset of Figure 5.5. Based on TGA measurements of three sections from each of the nancomposite specimen, the standard deviation in the residual weight was less than 0.2 vol. % in all cases, indicating attainment of well dispersed nanoparticles.
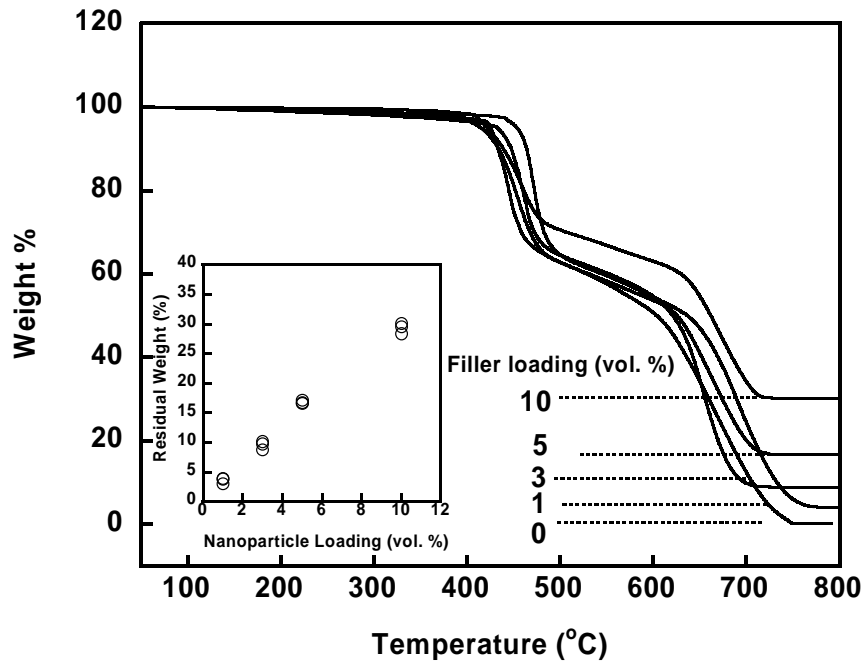
Figure 5.5: TGA measurements of BECy/ZrW$_2$O$_8$ nanocomposites at 20 ^{o}C/min. The residual weight of three sections of the nanocomposite specimen after heating to 850 ^{o}C are plotted as a function of filler loading in the inset.
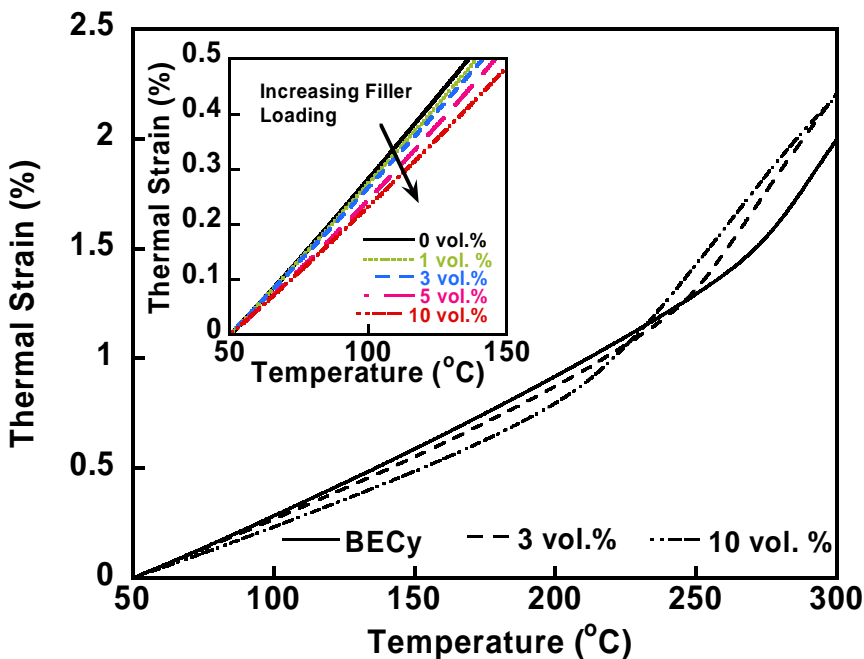
Figure 5.6: Representative curves demonstrating the effect of nanoparticle loading on thermal strain measured from TMA measurements. A magnified graph of the effect of filler loading on thermal strain of BECy is shown in the inset.

The relationship between thermal strain and temperature from TMA measurements is shown Figure 5.6 for the BECy/ZrW$_2$O$_8$ nanocomposites. The curves exhibit a gradual change in slope due to the onset of the glass transition and transformation of the material from a glassy to a rubbery state. The values of thermal strain are found to decrease systematically with filler loading, as demonstrated in the inset of Figure 5.6. The values of CTE can be estimated from the change in dimension of a material with temperature, as shown in Equation 1.

$$\alpha = \frac{1}{L_o}\frac{dL}{dT}$$
(1)

where L_o is the original length of the sample and dL/dT represents the change in length of the sample with temperature. The value of dL/dT between 50 to 100 ^{o}C was used to determine the value of glassy CTE for the nanocomposites in this work. The effect of ZrW$_2$O$_8$ nanoparticles on the CTE of the BECy are shown in Figure 5.7 as a function of filler loading. The average reduction in CTE for the BECy matrix is found to be 20 % upon incorporation of 10 vol. % filler. Upon considering a broader temperature range from 100 to 150 ^{o}C, the magnitude of CTE is still found to be 18.2 % upon incorporation of 10 vol. % filler. The values of glassy CTE obtained from experiments are compared against predictions from thermomechanical models [58-60] in Figure 5.7. The values of CTE in this work are found to be lower than the predictions from rule of mixtures, which considers the polymer matrix and the filler in terms of two separate phases, as shown in Equation 2 below:

$$\alpha_c = \alpha_f \varphi_f + \alpha_m (1 - \varphi_f)$$
(2)

where α_c is the CTE of the composite, α_f is the CTE of the filler (-8.7 ppm/^{o}C), α_m is the CTE of the polymer matrix (56.5 ppm/^{o}C), and φ_f is the volume fraction of the filler. The fact that the reduction in CTE obtained in this work is significantly better than the reduction predicted by the rule of mixtures is indicative of possible interactions between the matrix the nanoparticles. Schapery's model involves determination of upper and lower bounds of CTE using Equations 3 through 6 [58-61]:

$$\alpha_c^l = \alpha_m + \frac{K_f}{K_c^u}\frac{(K_m - K_c^u)(\alpha_f - \alpha_m)}{(K_m - K_f)}$$
(3)

$$\alpha_c^u = \alpha_m + \frac{K_f}{K_c^l}\frac{(K_m - K_c^l)(\alpha_f - \alpha_m)}{(K_m - K_f)}$$
(4)

where K_m represents the bulk modulus of the polymer matrix (2.06 GPa) and K_f represents bulk modulus of the filler (74.5 GPa). K_c^u and K_c^l refer to the upper and lower bound values of the composite bulk modulus and can be determined as shown in Equations 5 and 6:

$$K_c^l = K_m + \frac{1}{\dfrac{1}{K_f - K_m} + \dfrac{3(1 - \varphi_f)}{(3K_m + 4G_m)}}$$
(5)

$$K_c^u = K_f + \frac{1}{\dfrac{1}{K_m - K_f} + \dfrac{3\varphi_f}{(3K_f + 4G_f)}}$$
(6)

where G_m (0.78 GPa) and G_f (33.9 GPa) represent shear modulus of the matrix and filler, respectively. The values of CTE in this work are found to be in excellent agreement with the

upper bound of Schapery's model, which was also found to provide a good description of micron size ZrW_2O_8/BECy composites.
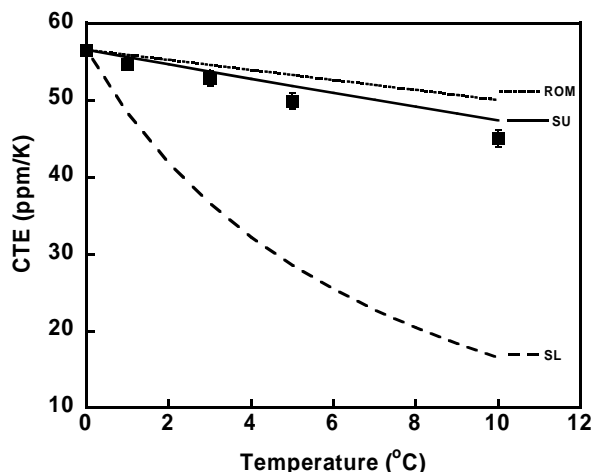
Figure 5.7: TMA measurements of the CTE for BECy/ZrW_2O_8 nanocomposites as a function of nanoparticle loading. ROM refers to CTE predicted based on rule of mixtures. SU and SL refer to the upper and lower bound CTE predictions based on Schapery's model. The error bars are standard deviations based on five measurements for each sample.
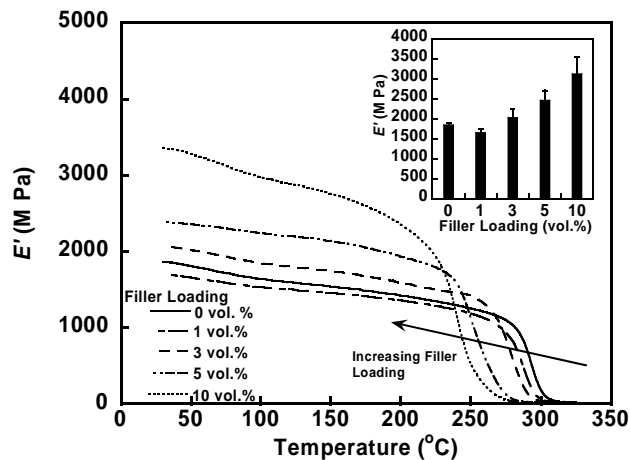
Figure 5.8: Representative curves demonstrating the effect of nanoparticle loading on the dynamic storage modulus (E') obtained from DMA measurements. A comparison of the average values of storage modulus from four measurements for each sample is shown in the inset as a function of filler loading.

The dynamic mechanical properties of the nanocomposite specimen are compared as a function of filler loading in Figure 5.8. The average values of the glassy storage modulus (E') is found to be 68 % higher for the 10 vol.% filler loading in comparison to the corresponding value for neat BECy, as shown in the inset of Figure 5.8. However, the storage modulus curves also appear to shift systematically to lower temperatures with increasing filler loading. The effect of the filler loading on the glass transition behavior of the nanocomposites can be characterized by comparing the onset temperature (T_{onset}) of the storage modulus curves, where the modulus values decreases rapidly with increasing temperature. The values of T_{onset} for BECy and the nanocomposites are plotted as a function of filler loading in Figure 5.9 and are found to decrease with increasing filler loadings. The decrease in T_{onset}, which is pronounced at higher filler loadings, is a manifestation of a decrease in the glass transition temperature of the nanocomposites with increasing filler loadings. In Chapter 3, it was shown that the presence of surface hydroxyl groups in micron size ZrW_2O_8 particles leads to early cure initiation and a reduction in T_g of BECy resin. However, silane surface treatment of the micron size particles decreased the catalytic effect and also substantially mitigated the extent of the T_g reduction even at loadings of 20 vol. %. Hence, the reduction in the T_{onset} observed in this work upon incorporation of 10 vol. % silane treated nanoparticles requires further examination. The effect of the ZrW_2O_8 nanoparticles on the cure reaction of BECy is demonstrated in Figure 5.10, through a comparison of cure exotherms obtained from DSC measurements. Upon incorporation of 10 vol. % unfunctionalized ZrW_2O_8 nanoparticles, a smaller exotherm can be observed between 100 ^{o}C and 150 ^{o}C prior to the actual cure exotherm, representing the early cure

initiation by the surface hydroxyl groups. The catalytic effect of ZrW_2O_8 nanoparticles on the cure behavior of BECy is significantly more pronounced than the effect observed upon incorporation of micron size ZrW_2O_8 particles. As shown in Figure 5.10, upon incorporation of 10 vol. % micron size ZrW_2O_8, the low temperature exotherm is not observed and the exotherm onset temperature, which represents the temperature where the reaction is initiated, is found to decrease by approximately 45 ^{o}C in comparison to BECy, for a heating rate of 10 ^{o}C/min. On the other hand, upon incorporation of 10 vol. % ZrW_2O_8 nanoparticles, the exotherm onset temperature decreases by 105 ^{o}C in comparison to the exotherm for BECy. The catalytic effect and early cure initiation as a consequence of filler loading can lead to changes in the crosslinked network structure of BECy and reduce the glass transition temperature of the matrix.

The dramatic catalytic effect is reduced through silane surface functionalization of the nanoparticles, which shifts the cure exotherm to higher temperatures, as shown in Figure 5.10. However, the onset and peak temperatures upon incorporation of 10 vol. % silane treated nanoparticles are still substantially lower than the corresponding neat BECy resin.
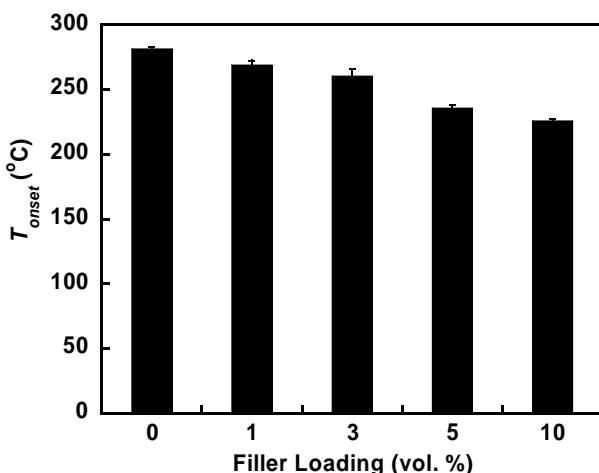
Figure 5.9: A comparison of the average values of the onset temperature of the storage modulus (T_{onset}) as a function of filler loading. The error bars are standard deviations based on four measurements for each sample.
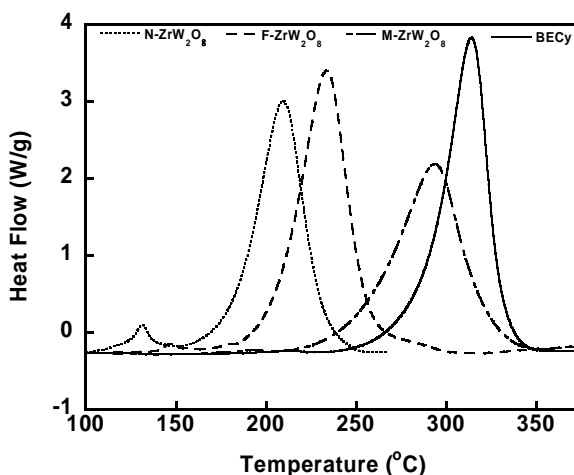
Figure 5.10: Effect of ZrW_2O_8 loading on the cure behavior of BECy resin.M- ZrW_2O_8, N-ZrW_2O_8, F-ZrW_2O_8 refer to BECy suspensions with 10 vol. % micron size, nanosize, and and silane treated ZrW_2O_8 nanoparticles, respectively.

In Chapter 3, the improvement in T_g as a consequence of silane surface treatment of micron size ZrW_2O_8 particles was attributed to enhanced compatibility of functionalized ZrW_2O_8 particles with BECy due to partial steric shielding of the hydroxyl groups. The increase in onset and peak temperatures upon incorporation of functionalized nanoparticles indicates that such a shielding effect does exist; however, the effect is considerably lower than the systems with micron size particles. Hence, considering the significantly higher catalytic effect of ZrW_2O_8 nanoparticles, a reduction in the onset of the glass transition is observed with increasing filler loadings, in spite of the silane surface treatment. The dramatic catalytic effect of the nanoparticles on the cure reaction of BECy, even after silane treatment could invoke changes to the crosslinked network structure (i.e. lower crosslink density), which in turn can diminish the extent of achievable CTE reduction. Mitigating the dramatic catalytic effect of the ZrW_2O_8 nanoparticles on BECy could

minimize changes to the crosslinked network structure of BECy during the cure process and facilitate development of BECy/ZrW$_2$O$_8$ nanocomposites with even more improved thermomechanical properties. However, at the highest filler loading in this work, the nanocomposites are still characterized by glass transition temperatures greater than 200 ^{o}C and low values of CTE For temperatures 50 to 150 ^{o}C, which indicates that they hold significant promise as matrix materials for high performance fiber reinforced composites.

5.4   Conclusions

Zirconium tungstate nanoparticles synthesized by a hydrothermal method were incorporated in a unique cyanate ester resin to develop polymer nanocomposites with tailored CTE values. The low viscosity of the BECy resin facilitated incorporation of up to 10 vol. % of the nanoparticles which resulted in a CTE reduction of 20 %. Based on DMA measurements, the dynamic glassy storage modulus of the nanocomposite with 10 vol. % nanoparticle loading was found to be 68 % higher when compared to BECy, suggesting a reinforcement effect. However, the onset temperature of the storage modulus curves shifts systematically to lower temperatures at higher filler loading signaling a decrease in the glass transition temperature. The origin for the decrease in the glass transition temperature could be attributed to a dramatic catalytic effect, which manifests in the form of a low temperature exotherm between 100 ^{o}C and 150 ^{o}C, for unfunctionalized nanoparticles. Although the silane surface treatment appears to mitigate the extent of early cure initiation, the onset and peak temperatures of the cure exotherms upon incorporation of the functionalized nanoparticles are still lower than that of neat BECy resin. In spite of the dramatic catalytic effect for filler loading of 10 vol. %, the BECy/ZrW$_2$O$_8$ nanocomposite exhibits a T_g greater than 200 ^{o}C and a CTE that is 20 % lower than neat BECy resin, which identifies these systems as promising candidates for high performance composites.

CHAPTER 6: Macro-Nano Hybrid Cyanate Ester Composites with Tailored Thermal Expansion

6.1   Introduction

Fiber reinforced polymer composites are enabling technologies in a wide range of applications from aerospace to microelectronics. Carbon fibers are an excellent choice as fiber reinforcements due to their lightweight and remarkable range of mechanical, electrical, chemical, and magnetic properties. High performance polymer composites are often fabricated by impregnating carbon fiber reinforcements with thermosetting polymer resins which are capable of withstanding elevated service temperatures. The composites are prepared by a curing process which transforms the thermosetting resin in to a rigid, highly cross-linked polymer. When the composite is cooled following the cure, the cured polymer matrix can contract significantly due to the typically high coefficient of thermal expansion (CTE) of polymeric materials. On the other hand, carbon fiber reinforcements exhibit very low or negligible shrinkage due to their very low CTE values. This mismatch in CTE and thermal expansion between the polymer matrix and the carbon fiber reinforcements leads to development of residual stresses in the composite and can lead to loss of dimensional stability and hinder fabrication of parts with precise dimensions. Furthermore, under repeated thermal cycling, the CTE mismatch between the matrix and the fiber reinforcements can lead to a significant buildup of residual stress and may eventually cause material failure.

A reduction in the CTE of the polymer matrix through incorporation of negative CTE nanoparticles can reduce the extent of mismatch in CTE between the polymer matrix and the fiber reinforcements, and also mitigate the magnitude of the residual stresses developed during composite processing. This chapter describes the development of unique hybrid composites with the BECy polymer matrix reinforced macro scale unidirectional carbon fibers and nano scale ZrW_2O_8 nanoparticles. Composites were prepared with both symmetrical and unsymmetrical layup in order to examine the effect of negative CTE filler loading. Composites with a 2 ply unsymmetrical layup were prepared in order to examine the effect of ZrW_2O_8 nanoparticle loading on the warpage of the composites following the cure. Composites with a 10-ply symmetrical layup were prepared in order to characterize the effect of ZrW_2O_8 nanoparticle loading on the thermomechanical properties of the composites

6.2 Methodology

6.2.1   Materials

The BECy resin used was EX 1510 resin obtained from Tencate Technologies (Morgan Hill, CA). The catalyst (EX 1510 B) required for curing the resin was also obtained from Tencate Technologies and added at a ratio of 3 parts catalyst per hundred parts resin. The unidirectional carbon fiber mats were obtained from FiberGlast Inc. (Brookeville, OH)

6.2.2 ZrW_2O_8 nanoparticle synthesis and functionalization

The nanoparticles were synthesized through the hydrothermal approach described in Chapter 4 and functionalized using the silane surface treatment method described in detail in Chapter 5.

6.2.3 Composite Layup and Processing

The carbon fiber mats were cut in to 3.5×3.5 in squares for 2- ply symmetrical or unsymmetrical composites and 1×1 in squares for 10-ply symmetrical composites. A desired amount of BECy and corresponding catalyst was then weighed out so as to achieve a 30 wt.% carbon fiber loading for both symmetrical and unsymmetrical composites after curing, assuming no loss in processing (discharge of BECy from the composite during cure was optimized to a negligible amount for these tests). The Catalyst EX1510-B, was added at a ratio of 3 parts catalyst to 100 parts BECy, as specified by the manufacturer. Required amount of functionalized ZrW_2O_8 nanoparticles were added to the neat BECy resin and the suspension was homogenized by ultrasonic mixing using a Branson 1510 Ultra Sonic Bath. Nanoparticles loadings of up to 10 vol. % (of resin) were prepared for the 2-ply unsymmetrical composites while loadings of up to 20 vol.% were used for symmetrical composites.

The nanocomposite suspensions were separated into equal amounts and applied to both sides of the carbon fiber plies. A ply was then laid individually in the desired orientation on Teflon paper and rolled with a lightweight plastic roller to attain even wetting before laying the next ply. A 0/90 orientation was employed for the 2 ply unsymmetrical composites while the layup for the 10-ply symmetrical composite was $(0/90/0/90/0)_2$. The composites were degassed under vacuum for thirty minutes.

The composites were placed on a hot press and heated to $160^{\circ}C$ and held isothermally for a few minutes to pre cure the resin and to prevent it from oozing out of the mold when under pressure. The pre cure time was 10 minutes for neat BECy resin while only 7 or 8 minutes of pre cure was required for the nanocomposite suspensions due to the catalytic effect of the ZrW_2O_8 nanoparticles. Following the short pre cure, pressure was then immediately applied and held constant at 150 lb/in^2 while the temperature was increased from 160 $^{\circ}C$ to180$^{\circ}C$, where the sample was held isothermally for two hours. The composite was then allowed to cool to room temperature still under pressure for three hours. The pressure was completely released once the sample had attained room temperature. Afterward the composite was post cured at 250$^{\circ}C$ for two hours in a convection oven under a pressure plate providing 2 lb/in^2 to achieve full cure and was subsequently cooled at 1° C/min back to room temperature.

6.2.4 Characterization

Scanning Electron microscopy was performed with a FEI Quanta FE SEM to examine the nature of the nanoparticle dispersion in the hybrid composites. The CTE of the 10 ply symmetrical composite samples were characterized in both normal and in-plane modes using a Q400 Thermomechanical analyzer from TA Instruments. In the normal mode, all the plies were aligned normal with respect to the TMA probe, while in the in-plane mode, certain plies were aligned parallel to the probe direction. The samples with approximate dimensions of $3 \times 3 \times 3$ mm were first heated at 5 $^{\circ}C$/min to 300 $^{\circ}C$ to erase previous thermal history. Following cooling at 5 $^{\circ}C$/min, a second heating scan at 5 $^{\circ}C$/min was performed to determine the CTE of the composites.

The effect of temperature on the warpage of the 2 ply unsymmetrical composites was characterized by analysis of images captured using a digital camera. The sample to be characterized was placed in the stage of temperature controlled oven with a clear glass window. One end of the sample was supported on the stage while the dimension change of the other end was monitored. A digital camera was mounted on a stand and aligned along the same level as the sample stage. The measurements were performed by heating the sample to temperatures

between 25 °C to 300 °C in intervals of 25 °C. The sample was allowed to equilibrate at each temperature for several minutes after which, three photographs were recorded. The photographs were analyzed using image processing software to determine the variation of curvature of the sample with temperature.

6.3   Results and Discussion

The SEM image of the fracture surface of a 10-ply hybrid composite is shown in Figure 6.1a. Images obtained at higher magnifications facilitate characterization of nanoparticle dispersion in the hybrid composites and are shown in Figures 6.1b through d.   The images reveal attainment of excellent levels of nanoparticle dispersion for all loadings employed in this work.

a)   b)   c)   d)
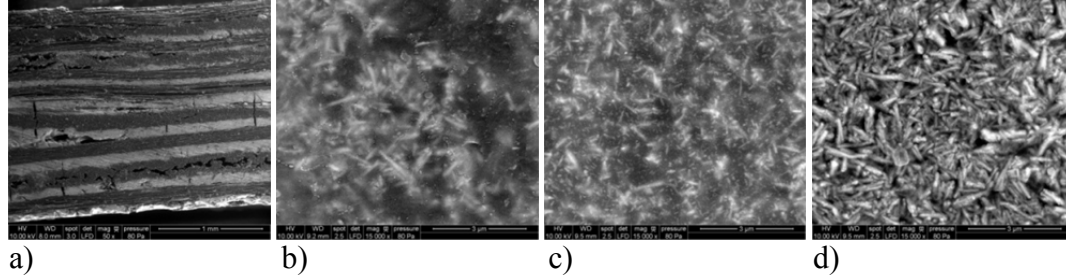
Figure 6.1: SEM images of a) Cross section of 10-ply hybrid composite b) Hybrid composite with 2.5 vol. % nanoparticles c) Hybrid composites with 10 vol. % nanoparticles d) Hybrid composite with 20 vol. % nanoparticles.

The relationship between thermal strain and temperature for the hybrid composites obtained from TMA measurements in the normal mode are shown in Figure 6.2. The thermal strain below the glass transition is found to decrease dramatically with nanoparticle loading, as shown in Figure 6.2. The values of CTE determined from the slope of the dimension change curves are plotted as a function of nanoparticles loading in Figure 6.3. The results reveal a systematic reduction in CTE with nanoparticle loading and a maximum reduction of almost 75 % upon incorporation of 20 vol. % nanoparticles.
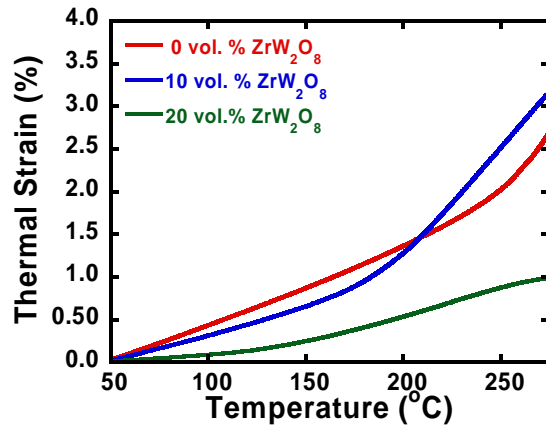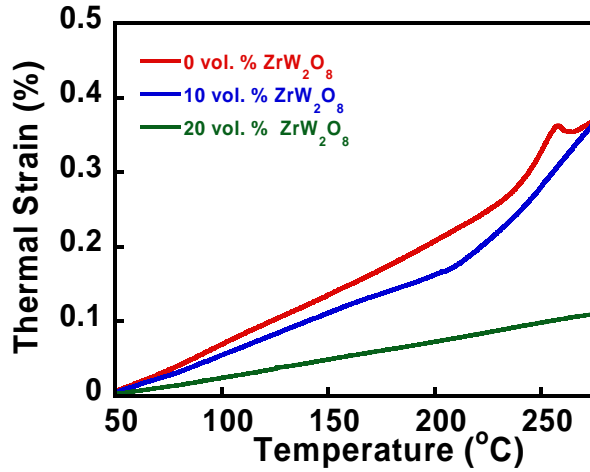

Figure 6.2: Relationship between thermal strain and temperature for the hybrid composites as a function of ZrW_2O_8 nanoparticle loading, when measured in the normal mode.
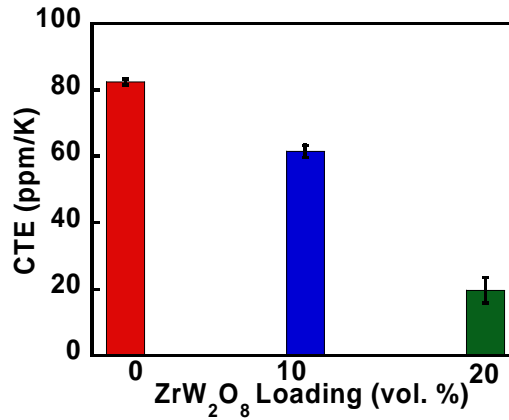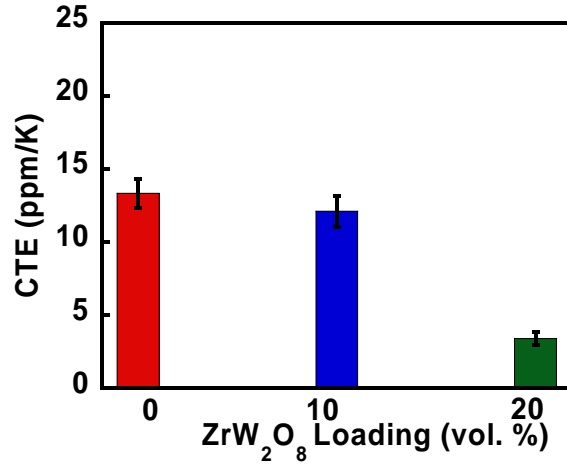
Figure 6.3: Relationship between CTE and ZrW_2O_8 nanoparticle loading when measured in the normal mode.

The thermal strain versus temperature curves obtained from TMA measurements in the in plane mode are compared as a function of nanoparticle loading in Figure 6.4. The thermal strain is found to decrease systematically with nanoparticle loading. The values of CTE obtained from the slopes of the curves shown in Figure 6.4 are plotted as a function of nanoparticle loading in Figure 6.5. For any level of nanoparticle loading, the values of CTE are lower for measurements from the in plane mode when compared to the measurements in the normal mode. This is not unexpected since the CTE of carbon fiber is around 15×10^{-6} K^{-1} in the normal direction and -0.5×10^{-6} K^{-1} in the parallel direction. The measurements in the in-plane mode also reveal a dramatic decrease in the CTE with nanoparticle loading. The maximum decrease in the CTE is found to be 75 % for a nanoparticle loading of 20 vol. %, also similar to the trends observed for the measurements in the in plane mode.


Figure 6.4: Relationship between thermal strain and temperature for the hybrid composites as a function of ZrW_2O_8 nanoparticle loading, when measured in the in plane mode.

Figure 6.5: Relationship between CTE and ZrW_2O_8 nanoparticle loading when measured in the in plane mode.

The extent of warpage following the cure due to the mismatch in CTE between the carbon fibers and the BECy matrix without any nanoparticles is shown for 2 ply unsymmetrical composite in Figure 6.6a. As shown in Figure 6.6b, a 2 ply symmetrical composite does not incur any warpage following the cure and is completely flat.
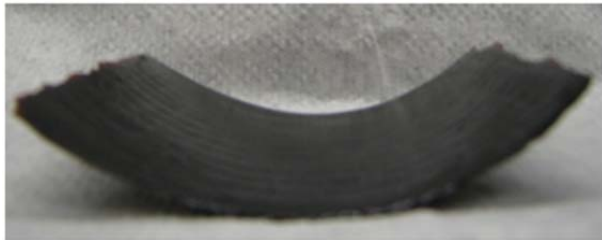

a)   b)

Figure 6.6: Image of 2 ply composites following the cure schedule a) unsymmetrical lay up b) symmetrical layup

The effect of nanoparticle loading of loading on the warpage of 2 ply unsymmetrical composites is shown in Figure 6.7. The unsymmetrical composites are supported on one edge to illustrate the effect of nanoparticle loading.   The extent of curvature for the unsymmetrical composites following the cure is found decrease systematically with filler loading.   The decrease in the extent of curvature following the cure is clearly a manifestation of the decrease in the extent of thermally induced residual stresses in the composites. However, the origin for the decrease in the extent of residual stresses in the case of the hybrid composites requires further examination.
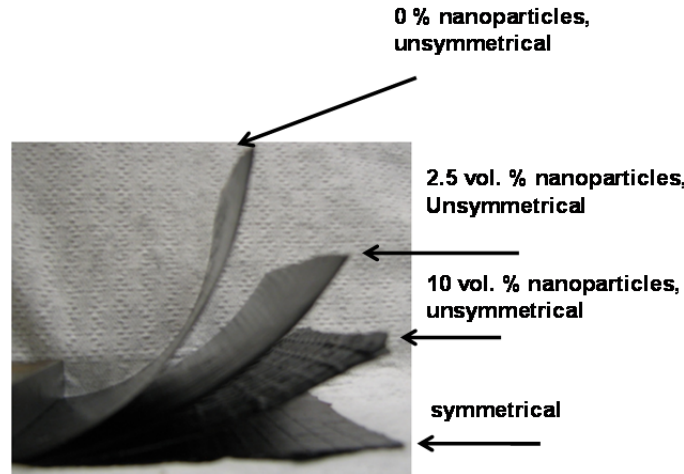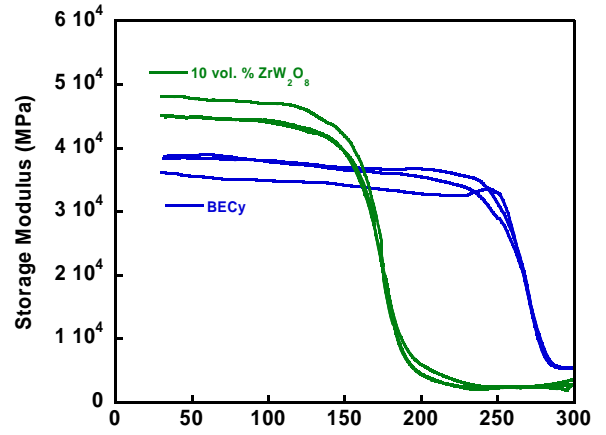

Figure 6.7: Effect of ZrW_2O_8 nanoparticle loading on the curvature or warpage of 2 ply unsymmetrical composites. A flat 2 ply symmetrical composite is included for reference.

The residual stresses (σ_r) generated in a composite can be expressed as shown in Equation 6.1 below:

$$\alpha_r \propto \left(T_g - T\right) \cdot \alpha_c \qquad (6.1)$$

where T_g is the glass transition temperature and α_c is the CTE of the composite. As shown in Figures 6.2 and 6.4, the CTE of the composites is reduced upon incorporation of the nanoparticles.   However, the values of T_g are also decreased with nanoparticle loading, as shown in Figure 6.8, by the shift in the onset points of the storage modulus curves to lower temperatures, as a consequence of nanoparticle loading. The composites do not experience any residual stress at temperatures above T_g and the stresses start developing as the materials cools down to temperatures in the vicinity of T_g. Consequently, a reduction in T_g could also mitigate the extent of

Figure 6.8: DMA measurements of symmetrical hybrid composites that demonstrate the effect of nanoparticle loading on T_g

residual stresses developed in the composite. Hence the effects of CTE reduction and T_g reduction need to be delineated to better understand the decrease in warpage exhibited by the unsymmetrical hybrid composites.

The effect of temperature on the curvature of unsymmetrical BECy/carbon fiber fiber composite is illustrated through the images in Figures 6.9a through d. As the temperature is increased the curvature of the composite decreases systematically and the composite is completely flat for temperature above T_g, as illustrated in Figure 6.9d. Upon cooling the sample from 300 $^\circ$C, the residual stresses develop once again, leading to a warped sample at room temperature.
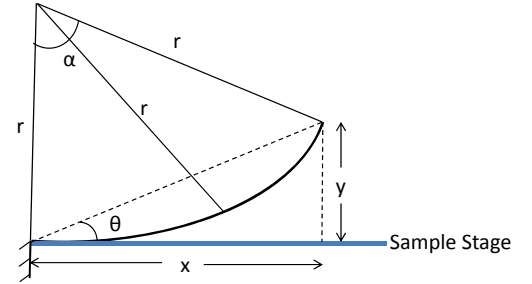

a)   b)   c)   d)
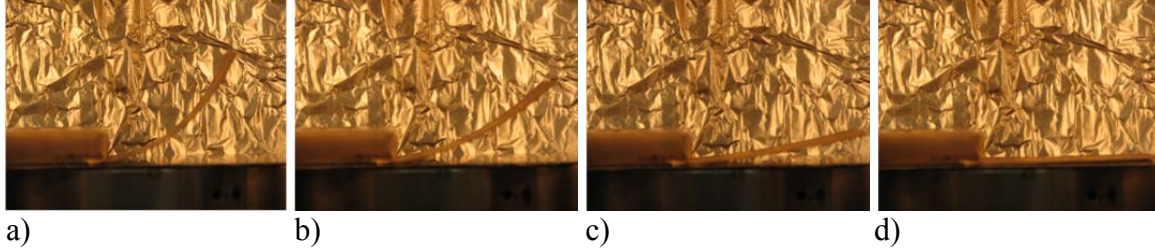
Figure 6.9: Effect of temperature on the curvature of 2 ply unsymmetrical composite a) T = 25 $^\circ$C b) T = 125 $^\circ$C c) T = 225 $^\circ$C d) T = 300 $^\circ$C

The photographs obtained at different temperatures for the unsymmetrical composite and the hybrid unsymmetrical composite with 10 vol. % nanoparticles were analyzed to determine the curvature of the composite specimen, as demonstrated in Figure 6.10. The composite panel could be considered as an arc of length L in a segment of radius r. By monitoring the change in the longitudinal (x) and vertical displacement (y) of the sample with temperature, the angle of curvature (θ) can be measured. The angle of the segment (α) can be determined by solving for Equation 6.2 shown below:
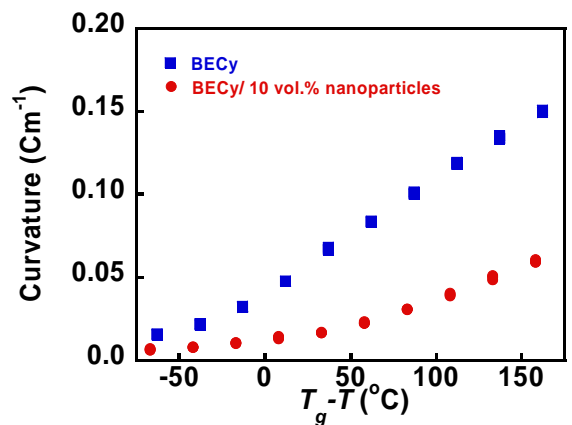

Figure 6.10: Schematic representation of curvature calculations for 2 ply unsymmetrical composites

$$\frac{1-\cos\alpha}{\sin\alpha} = \tan\theta \qquad (6.2)$$

Subsequently, the radius of the segment is obtained as r = L / α, while the curvature (κ) of the sample can be obtained as κ = 1/r .

The relationships between curvature and the distance from T_g (defined as T_g-T) is compared for the unsymmetrical composites with and without nanoparticles in Figure 6.11. At temperatures higher than T_g, (T_g-T) is negative and the curvature values approaches zero due to the presence of minimal or no residual stress. On the other hand, at temperatures lower than T_g, the curvature increases systematically with decreasing temperature, as expected. Figure 6.11 demonstrates that incorporation

Figure 6.11: Relationship between curvature and temperature for 2 ply unsymmetrical composites

of 10 vol. % nanoparticles results in lower curvature at any value of (T_g-T). In other words, at the same distance from the glass transition, the hybrid composite is characterized by lower magnitude of curvature. Hence, the decrease in the curvature for the hybrid composites is clearly a manifestation of the reduction in residual stresses as a consequence of the reduction in the CTE mismatch between the carbon fibers and the polymer matrix achieved through incorporation of nanoparticles.

6.4   Conclusions

In this work, hybrid composites with 30 wt. % unidirectional carbon fibers and various loadings of ZrW_2O_8 nanoparticles were prepared. The CTE of the 10 ply symmetrical hybrid composites was found to decrease upon incorporation of nanoparticles. A maximum reduction in CTE of 75 % was observed in either the in plane or the normal modes for a nanoparticle loading of 20 vol.%. The warpage or curvature following the cure of 2 ply unsymmetrical composites was also found to decrease systematically with nanoparticle loading. The temperature dependence of curvature was compared for the neat and hybrid composites in order to identify the reason for reduction in warpage. The results revealed that for any given distance from T_g, the hybrid composite exhibits lower curvature, which confirmed that the reduction in warpage was a direct consequence of mitigation of thermally induced residual stress due to the reduction in CTE mismatch between the polymer matrix and carbon fibers.

CHAPTER 7: Summary

This work discussed various stages in the development of unique hybrid composites with low CTE. Polymer composites and nanocomposites were developed with negative CTE fillers zirconium tungstate and multiwalled carbon nanotubes (CNTs). Baseline studies were conducted with bisphenol E cyanate ester (BECy) resin and micron size zirconium tungstate (ZrW_2O_8) particle to develop processing strategies and surface functionalization methods to ensure compatibility between the polymer matrix and the ceramic. ZrW_2O_8 nanoparticles were synthesized in different morphologies and were used to develop polymer nanocomposites with BECy resin. The BECy/ZrW_2O_8 nanocomposites were identified as the most promising candidates for the development of hybrid composites. The hybrid composites comprising of 30 wt. % unidirectional carbon fibers and various loadings of nanoparticles exhibited reduced CTE values and better dimensional stability as a consequence of reduced residual stresses. The important results and conclusions from various stages of this research work are highlighted below:

1. BECy/CNT nanocomposites were developed through incorporation of up to 1 wt. % pristine CNTs, OH functionalized CNTs, and COOH functionalized CNTs. Incorporation of 1 wt. % OH and COOH CNTs increased the impact strength of BECy by 91 % and 63 %, respectively. The CNTs exerted a significant catalytic effect on the cure reaction of BECy: a 40-55°C decrease in the onset temperature of the BECy cure exotherm upon incorporation of only 0.5 wt. % OH CNTs. The maximum reduction in CTE was around 2.5 % upon incorporation of 1 wt. % CNTs. Considering that significant processing difficulties can be encountered at higher filler loadings necessary to achieve greater CTE reductions, these nanocomposite systems were not used for hybrid composite development.

2. BECy/ZrW_2O_8 composites were developed with 10, 20 and 65 vol. % micron size ZrW_2O_8 particles to identify processing and surface functionalization strategies. Although, incorporation of ZrW_2O_8 facilitated, a systematic reduction in the CTE of the polymer matrix, the cure reaction of BECy was found to be catalyzed by the presence of surface hydroxyl groups in ZrW_2O_8, which also resulted in a decrease in the glass transition temperature (T_g). A silane surface treatment strategy was developed and found to be effective in mitigating the magnitude of reduction in T_g.

3. ZrW_2O_8 nanoparticles were synthesized using sol-gel and hydrothermal methods. The hydrothermal process was preferred for development of polymer nanocomposites due to its shorter processing times and also due to its ability to result in pure, uniform, ZrW_2O_8 nanoparticles.

4. BECy/ZrW_2O_8 nanocomposites were developed through incorporation of up to 10 vol. % silane treated ZrW_2O_8 nanoparticles. A maximum reduction in CTE of 20 % was observed for a nanoparticle loading of 10 vol. %. However, the reduction of CTE was also accompanied by a reduction in T_g, in spite of the silane surface treatment. The reduction in T_g was determined to be due to an even more dramatic catalytic effect in the case of ZrW_2O_8 nanoparticles in comparison to micron size ZrW_2O_8.

5. Hybrid composites were developed with 30 wt. % carbon fibers and various loading of ZrW_2O_8 nanoparticles. The CTE of symmetrical 10 ply composites was reduced by 75 % in the normal and in plane directions, for a nanoparticle loading of 20 vol. %. The warpage in 2 ply unsymmetrical composites was reduced upon incorporation of nanoparticles as a consequence of mitigation of the magnitude of residual stresses due to the reduction in extent of CTE mismatch between the carbon fibers and the polymer matrix.

References

[1]   B. Safadi, R. Andrews, E.A. Grulke. *J. Appl. Polym. Sci.* 84, 2660, **2002**.

[2]   F. Dalmas et al., *J. Polym Sci. Polym. Phys.* 43,1186, **2005**.

[3]   J. Njuguna, K. Pielichowski. *Adv. Eng. Mat.* 6, 204, **2004**.

[4]   D.A. Shimp, W.M. Craig Jr. *Proc. of the 34th Ann. SAMPE Symposium*, p 1336, May **1989.**

[5]   A.W. Snow. *Chemistry and Technology of Cyanate Ester Resins*, Blackie Academic and Professional, **1994**.

[6]   R. Hillermeirer, J. Seferis. *J. Appl. Polym. Sci.* 77, 556, **2000**.

[7]   S. Robitaille. *ASM Handbook - Composites*, Vol. 21, pp. 126, Materials Park, OH, **2001**.

[8]   I. Hamerton, J. Hay. *High Performance Polymers*, 10, 163, **1998**.

[9]   J.R. Esslinger, O.C. Fruchtnicht. *SAMPE Journal* 40, 9, **2004**.

[10]   S. Iijima. *Nature* 354, 56, **1991**.

[11]   S. Iijima, T. Ichihashi. *Nature* 363, 603, **1993**.

[12]   D.S. Bethune, et al. *Nature* 363,605,**1993**.

[13]   M-F. Yu, B.S. Files, S. Arepalli, R.S. Ruoff. *Phys. Rev. Lett.* 84,5552,**2000**.

[14]   H.R. Lusti, A.A. Gusev. *Modelling and Simulation in Mate. Sci. and Eng.*, 12, S107-S119, **2004**.

[15]   O. Breuer, U. Sundararaj. *Polymer Composites*, 25, 630, **2004**.

[16]   A. Allaoui, S. Bai, et al., *Compos. Sci. Technol.* 62, 1993, **2002**.

[17]   T. Ogasawara, Y. Ishida et al., *Composites Part A*, 35, 67, **2004**.

[18]   L. Zihong, *Proc. of the 50th Ann. SAMPE Symposium*, p 2331, May **2005**.

[19]   A.W. Sleight. *Ann. Rev. Mat. Sci.* 28, 29, **1998**.

[20]   J.D. Shi et al., *Proc of the Mater. Research Society Symposium,* 445, 229, **1997**.

[21]   W.C. Weyer. *Proc. of the 46th AIAA/ASME/ASCE/AHS/ASC Conf.*, 6, 3577, **2005**.

[22]   L.M. Sullivan, C.M. Lukehart. *Chem. Mater.* 17, 2136, **2005**.

[23]   W.M. Cross, et. al., Functional fillers and nanoscale materials: New markets and horizons,ed: J.J. Kellar, SME ,pp 127, 2006.

[24]   W.K. Goertzen, M.R. Kessler. *J. Therm. Anal. Calorim.* 93, 87, **2008**.

[25]   W. Miller, C.W. Smith, P. Dooling, A.N. Burgess, K.E. Evans. *Phys. Stat. Sol. B.* 245, 552, **2008**.

[26]   J.I. Tani, H. Kimura, K. Hirota, H. Kido. *J. Appl. Polym. Sci.* 106, 3343, **2007**.

[27]   S. Schnabel, W.M. Cross, J.J. Kellar, L. Kdjerentroen, J. Walsh. *SAMPE Proceedings*. 196/1, **2007**.

[28]   L. Zhang, J.Y. Howe, Y. Zhang, H. Fong. *J. Cryst. Growth and Design* 9, 667, **2009**.

[29]   X. Xing, Q. Xing , R. Yu, J. Meng, J. Chen, G. Liu. *Physica B* 81, 371, **2006**.

[30]   J.A. Colin, D.V. Camper, S.D. Gates, S.D. Simon, K.L. Witker, C. Lind. *J Solid State Chem.* 180, 3504. **2007**.

[31]   R. Andrews, M.C. Weisenberger. *Current Opin.Solid.St.M.* 8, 31, **2004**.

[32]   E.T. Thostenson, Z. Ren, T. Chou. *Compos. Sci. Technol.* 35, 95, **2004**.

[33]   X. Xie , Y. Mai, X. Zhou. *Mater. Sci. Eng. B* 119, 105, **2005**.

[34]   J. Wang, J. Chen, W.J. Blau. *J.Mater.Chem.*19, 7425, **2009**.

[35]   S.V. Ahir, Y.Y. Huang, E.M. Terentjev. *Polymer* 49, 3841, **2008**.

[36]   L. Bokobza. *Polymer* 48, 4907, **2007**.

[37] J. Wang, G. Liang, H. Yan, S. He. *Polym.Eng.Sci.* 49, 680, **2009**.

[38] D. Puglia, L. Valientini, I. Armentano, J.M. Kenny. *J.Appl.Polym.Sci.* 88, 452, **2003**.

[39] L. Guadagno, C. Naddeo, V. Vittoria, A. Sorrention, L. Vertuccio, M. Raimondo, V. Tucci, B. De Vivo, P. Lamberti, G. Lannuzzo, E. Calvi , S. Russo. *J.Nanosci. Nanotechnol.* 10, 2686, **2010**.

[40] T.L. Zhou, X. Wang, H.G. Zhu, T.C. Wang. *Compos. Part A- Appl. S.* 40, 1792, **2009**.

[41] A.D. La Vega, J.Z. Kovacs, W. Bauhofer, K. Schulte. *Compos.Sci.Technol.* 69, 1540, **2009**.

[42] H. Xie , B. Liu, Z. Yuan, Z. Shen, R. Cheng. *J.Polym.Sci.Polym.Phys.*42, 3701, **2004**.

[43] J. Bae, J. Jang, S.H. Yoon. *Macromol.Chem.Phys.* 203, 2196, **2002**.

[44] M. Abdalla, D. Dean, P. Robison, E. Nyairo. *Polymer* 49, 3310, **2008**.

[45] A. Allaoui, N. El Bounia. *Exp. Polym. Lett.* 3, 588, **2009**.

[46] Y.S. Tang, J. Kong, J.W. Gu, G.Z. Liang. *Polym.Plast.Technol.*48, 359, **2009**.

[47] A. Fanleib, L. Bardash, G. Boiteux. *Exp. Polym. Lett.* 3, 477, **2009**.

[48] H.P. Boehm. *Carbon* 32, 759, **1994**.

[49] B. Wetzel, F. Haupert, K. Friedrich, M.Q. Zhang, M.Z. Rong. *Polym. Eng. Sci.* 42, 1919 **2002**.

[50] J. Wang, G. Liang, H. Yan, S. He. *Polym.Eng.Sci.* 49,680,**2009**.

[51] J. Wang, Z. Fang, A. Gu, L. Xu, F. Liu. *J.Appl.Polym.Sci.* 100, 97, **2006**.

[52] W. Armstrong, M. Ruether, F. Blighe, W. Blau. *Polym. Int.* 58, 1002, **2009**.

[53] Y. Maniwa, R. Fujiwara, H. Kira, H. Tou, E. Nishibori, M. Takata, Sakata M, A.Fujiwara X. Zhao, S. Iijima, Y. Ando. *Phys.Rev.B.* 64, 073105,**2001**.

[54] S.M. Yuen, C.C. Ma, H.H. Wu, H.C.Kuan, W.J. Chen, S.H. Liao, C.W. Hsu, H.L. Wu. *J. Appl. Polym. Sci.* 103, 1272, **2007**.

[55] J.S.O. Evans, Z. Hu, J.D. Jorgensen, D.N. Argyriou, S. Short, A.W. Sleight. *Science* 275, 61, **1997**.

[56] J.D. Jorgensen, Z. Hu, S. Teslic, D.N. Argyriou, S. Short, J.S.O. Evans, A.W. Sleight. *Phys Rev B.* 59, 215, **1999**.

[57] J. Qiu, C. Zhang, B. Wang, and R. Liang *Nanotechnology* 18, 275708, **2007**.

[58] W.K. Goertzen, M.R. Kessler. *J. Appl. Polym. Sci.* 109, 647, **2008**.

[59] C.P. Wong, R.S. Bollampally. *J. Appl. Polym. Sci.* 74, 3396, **1999**.

[60] H.T. Vo, M. Todd , F.G. Shi, A.A. Shapiro, M. Edwards. *Microelectr. J.* 32, 331 **2001**.

[61] R.A. Schapery. *J. Compos. Mater.* 2, 380, **1968**.

[62] F.R. Drymiotis, H. Ledbetter, J.B. Betts, T. Kimura, J.C. Lashley, A. Migliori, A.P. Ramirez, G.R. Kowach, J. Van Duijn. *Phys. Rev. Lett.* 93, 25502-1, **2004**.

[63] X. Sheng, M. Akinc, M.R. Kessler. *Polym. Eng. Sci.* 50,302,**2010**,.

[64] I. Harismendy, C.M. Gomez, M. Del Rio, I. Mondragon. *Polym. Int.*, 49, 735, **2000.**

[65] C.M. Gomez, I.B. Recalde, I. Mondragon, I. *Eur. Polym. J. 41, 2734,* **2005.**

[66] W.K. Goertzen, X. Sheng, M. Akinc, M.R. Kessler, *Polym. Eng. Sci. 48*, 875, **2008.**

[67] X.G. Zheng, H. Kubozono, H. Yamada, K. Kato, Y. Ishiwata, C.N. Xu, *Nature Nanotechnology* 3,724, **2008**.

[68] I.B. Krynestskii, B.A. Gizhevskii, S.V. Naumov, E.A. Kozlov. *Phys Solid State* 50, 756, **2008.**

[69] W.H. Li, S.Y. Wu, C.C. Yang, S.K. Lai, K.C. Lee,H.L. Huang, H.D. Yang. *Phys Rev Lett* 89,135504/1, **2002.**

[70] J.S.O. Evans, J.D. Jorgensen, S. Short, W.I.F. David, R.M. Ibberson, A.W. Sleight. *Phys Rev B* 60, 14643, **1999**.

[71] T.A. Mary, J.S.O. Evans, T. Vogt, A.W. Sleight. *Science* 272, 90, **1996**.

[72] G.R. Sharma, M.R. Coleman, C. Lind. *40th ISTC Proceedings* **2008**.

[73] L.C. Kozy, M.N. Tahir, C. Lind,W. Tremel. *J. Mater. Chem.*19,2760, **2009**.

[74] N. Banek, H.I. Baiz, A. Latigo, C. Lind. *J. Am. Chem. Soc.* 132, 8278, **2010**.

[75] T.R. Ravindran, A.K. Arora, T.A. Mary, *Phys Condens Matter* 13,11573, **2001**.

[76] E.J. Liang, S.H. Wang, T.A. Wu, M.J. Chao, B. Yuan, W.F. Zhang, *J Raman Spectrosc* 38,1186, **2007**.

[77] L. Zhang, J.Y. Howe, Y. Zheng, H. Fong. *Cryst Growth Design* 9, 667, **2009**.

[78] R.F. Feldman, P.J. Sereda. Proceedings of International Symposium on Humidity and Moisture, Washington D.C. 4, 233, **1963**.